

TECHNOLOGY DEVELOPMENT FOR EXOPLANET MISSIONS

Technology Milestone Report
NASA Grant No. NNX10AF83G

JPL Document D-74384

ADVANCING TECHNOLOGY FOR STARLIGHT SUPPRESSION VIA AN EXTERNAL OCCULTER

PROF. N. JEREMY KASDIN
PRINCIPAL INVESTIGATOR
PRINCETON UNIVERSITY
MECHANICAL AND AEROSPACE ENGINEERING

September 28, 2012

CoInvestigators:

David N. Spergel (Science PI), Princeton University, Robert Vanderbei, Princeton University, Stuart Shaklan (Institutional PI), Jet Propulsion Laboratory, Julie Mikula (Institutional PI), NASA Ames Research Center, Bruce Macintosh (Institutional PI), Lawrence Livermore National Laboratory, Robert Rudd, Lawrence Livermore National Laboratory

Other Key Personnel:

Doug Lisman, Mark Thompson, Phillip Walkemeyer, Vinh Bach, Stefan Martin, Eric Cady, Jet Propulsion Laboratory, Dmitry Savransky, Lawrence Livermore National Lab

Approvals

Released by:



07/18/2012

N. Jeremy Kasdin
Principal Investigator, Princeton University

Approved by:



9/19/2012

Peter R. Lawson
Exoplanet Exploration Program Chief Technologist, JPL



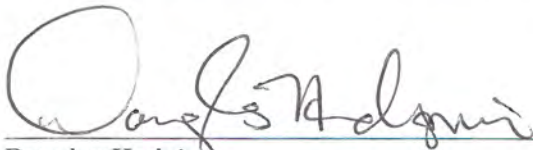
9/19/2012

Marie Levine
Exoplanet Exploration Technology Manager, JPL



9/20/2012

Peter Lawson
Exoplanet Exploration Program Manager (Acting), JPL



9/26/2012

Douglas Hudgins
Exoplanet Exploration Program Scientist, NASA HQ



9/26/2012

Lia LaPiana
Exoplanet Exploration Program Executive, NASA HQ

CONTENTS

1. Executive Summary	4
Major Accomplishments	4
Secondary Accomplishment	5
2. Certification	5
3. Success Criteria	6
4. Overview	7
4.1. Occulter Design Summary	7
4.2. Error Budget and Requirements Summary	8
4.3. Mechanical Design Summary	11
5. As-built Petal Manufacture and Assembly	12
5.1. Material Selection	13
5.2. Manufacturing Process	13
5.3. Optical Edge Metrology and Installation	14
6. Assembled Petal Shape Metrology	26
7. Contrast Calculation	29
7.1. Milestone Contrast Calculation	29
7.2. Performance Estimation for Non-Identical Petals	32
8. Material Coupon Testing	38
9. Conclusions, Lessons Learned and Future Work	41
9.1. Lessons Learned	41
9.2. Future Work	41
10. Acknowledgement	42
Appendix A. Success Criteria from Whitepaper	42
Appendix B. Allied Measurement Calibration and Statistical Modeling	43
B.1. Calibration data	43
B.2. Shape error distributions consistent with measurements	43
Appendix C. Material Selection and Testing	47
C.1. Overview	47
C.2. Sample Specification	47
C.3. Bending Tests	47
C.4. Optical Microscopy	48
C.5. Acoustic Tomography	50
C.6. Small-Angle X-Ray Scattering (SAXS)	52
C.7. Transmission Electron Microscopy (TEM)	54
C.8. Conclusions	54
Appendix D. Complete Error Budget	55
Appendix E. Table of Acronyms	56
References	57

1. EXECUTIVE SUMMARY

In this final report, we document the results of our ROSES Technology Development for Exoplanet Missions (TDEM) two-year research program to advance the technology associated with external occulter manufacturing and test. Our goal has been to advance the readiness of the riskiest key technology associated with occulter-based planet finding and characterization—manufacturing a large starshade to the needed accuracy. To that end we, for the first time, built a full-scale occulter petal, using flight-like processes and materials, and to near-flight tolerances as they are presently understood. We then performed metrology to confirm that the critical shape requirements had been met and our contrast goal achieved. We described the occulter optical design, the petal mechanical design and manufacturing process, the materials selection, the error analysis and requirement allocation, and the various modeling tools we use in the Technology Milestone Whitepaper, JPL Document D-68672, January 24, 2011. We will refer to that often in this report.

We show in this report that a precision starshade petal can be manufactured to meet the shape requirements summarized in the whitepaper and updated below and that its measured shape supports a preliminary derived error budget that is consistent with external occulter coronagraphs achieving our targeted contrast ratio development goal. To accomplish this, we simulated a full starshade populated by petals identical to the manufactured one. We then used our optical modeling tools to propagate an incident field to the image plane of the telescope and predict the resulting contrast. We repeated a sufficient number of times to give us statistical confidence in our predicted contrast. We chose a relaxed requirement from flight of 10^{-9} total contrast (3×10^{-10} allocated to manufacturing) as our success criterion as this is the first time any petal will have been built to flight tolerances, making a relaxed requirement appropriate.

As a reference, our milestone from the whitepaper is:

TDEM Occulter Milestone:

- On a single full-scale petal made of flight-like materials, measure the edge position relative to a fiducial origin at a sufficient number of locations along the edge. Using our optical modeling tools, verify that the predicted mean contrast in the image plane from a uniform field propagated past an occulter with petals of the measured shape in an annulus of width equal to the full-width half-max of the telescope point spread function at the smallest inner working angle is 3×10^{-10} or better, the allocated contrast to static errors. Repeat the measurements and analysis a sufficient number of times to give 95% confidence that the predicted contrast is correct.

Our accomplishments against the milestone are summarized below:

Major Accomplishments.

- (1) We successfully manufactured, assembled, and measured a full-size occulter petal out of flight-like materials using close to flight-like processes. Metrology results show the shape meets the requirements in the error budget for a flight-quality occulter.
- (2) We did better than the milestone for contrast from a modeled occulter made of up petals with the same measured shape. The expected value of the contrast from an occulter made up of 30 petals identical to the as-built petal is better than 2.15×10^{-10} at the smallest inner working angle and at all wavelengths of interest. Using a statistical analysis of the measurement error, we have 95% confidence that the contrast is better than 2.16×10^{-10} for the worst case wavelength, 30% better than our milestone value.
- (3) We showed that the more realistic case of an occulter made up of 30 petals with random manufacturing errors consistent with those seen in our measured as-built petal results in an expected contrast of 2.12×10^{-11} with a 95% confidence value of 4×10^{-11} at the worst case wavelength.

Secondary Accomplishment.

- (1) We measured microcracking in composite coupon samples undergoing strains similar to those experienced in the stowed occulter petal. No large cracks were found (> 100 microns) in either critical or non-critical structural elements for strains up to the maximum required level of 0.5% strain. Analysis is ongoing to quantify nanocracking at lower strain.

There were several secondary goals described in the whitepaper that we did not accomplish. Foremost was work on the precision, tapered optical edge. As described in the whitepaper, a precision optical edge serves to both determine the final optical width of the petal as well as to ensure solar scattering is minimized. While the final occulter as-built did have a precise edge that met the shape requirements, it did not have the sharp taper needed to minimize scatter. As we explained in the whitepaper, we had hoped, on a best effort basis, to develop manufacturing concepts for producing sharp edges and to test the scatter from edge coupons at NASA Ames on a best effort basis, without committing to specific metrology as part of this milestone. Unfortunately, the design and development work proved beyond the scope of the resources available and would have delayed or distracted from the primary objective. We also had concerns that available metrology would be ineffective with the sharp edge. (In a future development program we would expect that a more sophisticated laser metrology system would be used.) We therefore opted for a straight, vertical edge in the as-built petal. Work on tapering and other manufacturing concepts for the sharp edge continues under other support.

We had hoped that resources would allow a stow and deploy test of the as-built petal with additional post-deployment metrology. Unfortunately, we were not able to conduct such a test with the funding available.

We discuss in the whitepaper our integrated modeling approach to analyze the performance of an occulter with petals of the design built. In particular, we hoped to perform an optical-thermal-mechanical analysis of the occulter using measured coefficients of thermal expansion (CTEs) from coupons of the material used. Unfortunately, that had to be de-scoped from the TDEM project to free-up resources for the main milestone task. Nevertheless, preliminary analysis performed early in the project with reasonable estimates of CTEs for a TDEM petal used at a solar incidence angle of 85 deg (the coldest case with the most shadowing) showed the expected contribution of thermal effects to the image plane contrast to be no more than 10^{-11} at the inner working angle. Thermal-mechanical modeling work continues under other support.

2. CERTIFICATION

In this section, we reference the list of items for the certification data package from Section 5 of the milestone whitepaper and identify where they can be found in this report. The certification item description from the whitepaper is given in italics followed by the reference information in roman type.

- (1) *A narrative report, including a discussion of how each element of the milestone was met, and a narrative summary of the overall milestone achievement.*

This narrative report responds to item (1) of the certification data package.

- (2) *Description of petal design and materials and assembly steps.*

See Sections 4.3 and 5.

- (3) *Description of the measurement arm, precision stylus, and calibration certification data (provided by FARO Inc.)*

Note that this certification item was written when we expected to be using the FARO measurement arm for the final metrology. Instead, final metrology was done at Allied Mechanical; the measurement description is given in Section 6 and the calibration data is given in Appendix B. The FARO was used for short range measurements during installation

and was calibrated against the buttons measured by Allied. Accuracy data for the three coordinate measuring machines (CMMs) used in the project (Hexagon, Allied, and FARO at JPL) are given in Table 3. The Hexagon machine was certified on 5/2/2011, the Allied machine on 8/22/2011 and the FARO arm on 3/29/2007. External certification data are available on request.

The stylus description is given in Section 5.3.3.

- (4) *Description of the metrology process including the process for transferring the base and related intermediate data products, the (x,y) data along the petal edges, and estimates of repeatability.*

See Section 6 for a description of the final metrology process for the petal shape and Section 5 for descriptions of how the base coordinates were transferred and the intermediate data products were used. Appendix B discusses how we estimated the repeatability and came to estimates of the probability distribution of the measurements.

- (5) *Description of the model fitting process and results including error estimates and best fit rms petal shape to the measurements of the petal edge.*

Section 7 describes how we performed model fitting and developed error estimates of the best fit petal shape. It also describes how we converted that to contrast calculations.

- (6) *An updated error budget based on the measured petal shape. We will compute the likely contrast achieved assuming the measured petal shape is representative of the global and single-petal errors.*

The updated error budget is described in Section 4.2.

- (7) *A calculated image plane pattern assuming global and single-petal errors comparable to those measured on the actual petal.*

The final calculated image plane pattern based on the measured data for global petal errors is given in Section 7.1 and that for single-petal errors is given in Section 7.2.

- (8) *If time and resources allow, results of optical edge scatter tests.*

Time and resources did not allow for optical edge scatter tests.

3. SUCCESS CRITERIA

Appendix A reproduces verbatim the success criteria from the milestone whitepaper. Here we reference those criteria and indicate where in this report evidence of success or a description of the process can be found.

- (1-3) A description of the final measurements of the petal edge can be found in Section 6. A discussion of the measurement error and how we use it to estimate bounds on contrast is in Appendix B. The coordinate system used and how measurements were transferred to the global frame using the buttons is in Section 5.3.1.
- (4) When writing the whitepaper we had assumed that final measurement of the petal shape would be done with the FARO arm at JPL. Because of the large error and uncontrolled environment, we had concerns about repeatability and accuracy, which led us reconsider our approach. Subsequent to starting the project we made the decision to perform the final edge measurements at Allied Mechanical (as described in Section 6). The Allied machine had substantially better accuracy and precision, well within our milestone requirements, and the facility proved to be extremely stable (temperature variations of less than 2° C over 24 hours). This obviated the need to separate measurements by 24 hours, which would have been prohibitively costly. We performed 5 measurements at Allied rather than three (two were intended as calibration and setup but the quality was sufficient to use in the analysis). Inspection of the measurements after each run showed they were repeatable and consistent with the machine precision. All measurements occurred over 24 hours on February 7 and 8, 2012. The first two calibration runs were completed at 9:36 pm and 11:06 pm. The three

data runs took place between midnight and 5:00 am of the 8th, finishing at 1:31 am, 3:22 am, and 5:12 am.

- (5) The errors in fitting the petal shape to the final Allied edge measurements are described in Section 7.2. These are compared to the error budget in Section 4.2.
- (6-8) A complete description of the modeling tool for transforming the edge measurements to contrast and the resulting contrast estimation at a series of wavelengths is given in Section 7. This includes a statistical analysis of the measurements and how we build a probability density function for contrast. We demonstrate that hypothesis testing indicates success at meeting the milestone. Section 7.1 describes the contrast estimation and confidence level for a spinning occulter made of 30 petals identical to the as-built TDEM petal. Section 7.2 describes the contrast estimation and confidence level for a spinning occulter made of 30 petals with random edge errors consistent with those measured on the as-built TDEM petal. In the former case we performed better than the milestone by more than 30%. In the latter case, the 95% confidence value of contrast was more than a factor of 5 better than the milestone.

4. OVERVIEW

4.1. Occulter Design Summary. The technology whitepaper provides the background on occulters for exoplanet imaging; we will not repeat it here for brevity. Our approach to designing occulters uses optimization tools to determine the apodization that results in the smallest and closest possible occulter while still achieving the starlight suppression requirement over a desired wide spectral band.[1] We also place a premium on finding the smallest possible occulter. This makes it easier to manufacture and handle, reduces the size of the launch vehicle and fairing, and increases the potential science yield. Hence, the requirements we describe in the whitepaper and here are the tightest possible, specifying the allocated contrast at the smallest inner working angle (IWA) of the smallest possible occulter. (Making larger occulters for the same science objectives results in relaxed tolerances.)

The whitepaper also describes our approach to designing two-distance occulters, where different wavelength bands are imaged at different distances. This further allows a reduction in the size of the occulter. We describe a number of mission concepts at various scales for which we have designed and analyzed occulters. For this study, we have modified our O₃ design¹ to incorporate a 1.5 m telescope, thus making the image plane contrast slightly less sensitive to occulter errors and easier to fit in the facility. The resulting two-distance occulter, dubbed DI22 and shown in Figure 1, is 32 m in diameter with 6 m long petals and a slightly larger inner working angle than a flagship size mission such as *THEIA*,² 90 mas rather than 75 mas. It operates over the same pair of wavelength bands as O₃: 250-550 nm at a distance of 36670 km and 500-1100 nm at a distance of 18335 km. We have also designed the occulter for 30 petals to lower the cost and simplify the manufacturing for this first test. With 30 petals, each petal has the desired length and a width at the widest point of 2.34 m, which makes it more manageable for our existing facilities. This comes at the expense of smaller gaps between petals and narrower tips (1 mm). An eventual flight design would most likely have fewer, but wider, petals (as few as 16) with correspondingly larger gaps and tips (up to 2 mm).

¹O₃, or the Occulting Ozone Observatory, was a mission concept for a 1.1 m telescope and 30 m tip-to-tip occulter with 24 7.5 m long petals. It had the capability to detect planets down to Earth size, perform photometric characterization, detect the present of ozone, and do general astrophysics. [2, 3]

²*THEIA*, the Telescope for Habitable Exoplanets and Interstellar/Intergalactic Astronomy, is a flagship size mission concept developed as part of NASA's Astrophysics Mission Concept Studies in 2009. It consists of a 4-meter on-axis optical/UV telescope with an external occulter for planet detection and characterization.[4] The *THEIA* occulter is 40 m in diameter, with 20 petals, and is designed to work in two wavelength bands at different locations from the telescope: the 250-700 nm band at 55000 km, and the 700-1000 nm band at 35000 km.

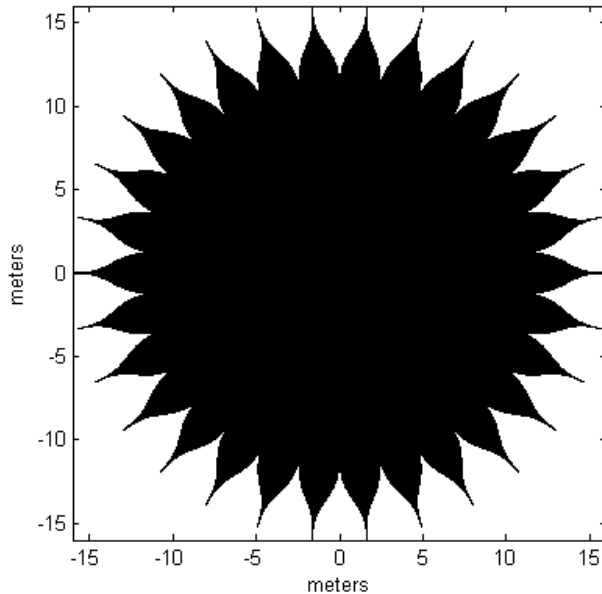


FIGURE 1. The DI22 occulter designed for a 1.5 m telescope being used for this TDEM study. It is 32 m in diameter with 30 petals, each 6 m long and 2.34 m wide at the widest point.

4.2. Error Budget and Requirements Summary. As stated in the certification section in the whitepaper, we have updated the error budget to better represent the construction process and errors encountered in the building and measuring of the TDEM petal. In particular, before building the petal we had modeled petal shape perturbations as ideal edge segment displacements and tilts combined with sine waves running the length of the petal, in addition to global size and shape errors. [5] After building the petal using high-precision ($5\mu\text{m}$) metrology to define fiducials along the edge, we found that it was no longer necessary to carry sine wave errors along the full petal length; rather, we have replaced them with sine wave shape errors on each of the segments. We also found that contrary to our initial expectations, global petal errors are unlikely to play a significant role in the error budget. We initially thought that our prediction of contrast would be limited by our metrology, suggesting that global systematic errors could be a problem. However, our experience showed (as will be highlighted in later sections) that the residual contrast is dominated by construction and assembly errors, which are expected to be random. This is largely due to our change from using the FARO measuring arm to a coordinate measuring machine (CMM) at Allied mechanical, which will be described in more detail below. As a result, the updated error budget we describe in this section mainly considers random errors from petal-to-petal, not global ones. Nevertheless, because the milestone specifies that we compute contrast for an occulter composed of identical petals, we still do so; that is described in Section 7.1. Fitting the measured edge segments to the error budget terms and computing the contrast for an occulter made of random petals is described in Section 7.2.

The error budgeting tool is an Excel spreadsheet that reads sensitivity files generated from propagation models. We compute the image plane mean and r.m.s. contrast for a given amplitude of each perturbation (e.g., a $100\mu\text{m}$ sine wave of 3 cycles per segment on segment 1) over a $1\lambda/D$ annulus centered at the inner working angle and evaluate at 7 wavelengths spanning the starshade bandpass ($0.25\text{--}0.55\mu\text{m}$ for the TDEM starshade) assuming a Gaussian distribution of error. The contribution of a given perturbation to the residual contrast scales as the square of the perturbation

Perturbation	Amplitude (1σ)	Contrast	Wavelength (nm)
Segment δx	100 μm	1.3×10^{-11}	550
Segment δy	100 μm	1.65×10^{-10}	550
Segment In Plane Tilt	100 μrad	4.1×10^{-11}	550
1 cycle/segment	100 μm	4.6×10^{-10}	300
2 cycle/segment	100 μm	3.4×10^{-11}	300
3 cycle/segment	100 μm	2×10^{-11}	250
4 cycle/segment	100 μm	8.1×10^{-11}	250
5 cycle/segment	100 μm	4.4×10^{-11}	250
6 cycle/segment	100 μm	2.8×10^{-10}	250
Proportional Width	1×10^{-5}	2.8×10^{-13}	550
Tip Clip	10 mm	1.15×10^{-11}	250
Quadratic Out-of-Plane Bend	5 mm	6.3×10^{-15}	550
Quadratic in-Plane Bend	0.25 mm	1×10^{-16}	550

TABLE 1. Contrast sensitivities to top 13 most significant manufacturing errors on petal edge segment shapes. All errors are zero mean. Amplitude numbers are 1σ deviations. Contrast is expected value of contrast for each individual perturbation based on a Gaussian distribution with given 1σ standard deviations.

amplitude. We treat all perturbations as independent and combine the coherent background scatter, local (speckle-like) scatter, and radially symmetric scatter following the approach described in Shaklan et al (2010). [6] Table 1 shows the resulting sensitivities for the top 13 most significant perturbation terms in the error budget.³ This includes segment x and y displacement (where x is defined as parallel to a line connecting the segment end points and y is orthogonal to this in the plane of the petal), in-plane tilt of the segment, and sine and cosine waves running along the segments. The table also indicates the worst-case wavelength where the contrast sensitivity was evaluated. Contrast values given are the average scatter level assuming a spinning starshade and all 30 petals with different (random) errors selected from the Gaussian distribution.

In addition to the segment placement and shape errors, we also consider proportional width and in-plane and out-of-plane quadratic bends on the petals. The proportional width error was originally conceived to account for long-range metrology errors that could be significant over the width and length of the petal, and smaller closer to the tip of the petal. We have found that the combination of the high-precision metrology used to define the petal mechanical structure with small-distance metrology used to place the segments (that is, we measured only from mechanical edge fiducials to nearby optical edge fiducials) prevented the buildup of significant proportional width errors. As described in Section 5.3.2 the runout errors in the CMM used to define the optical edge were less than $\sim 5\mu\text{m}$. The metrology used to determine placement of the optical edges was accurate to $\sim 10\mu\text{m}$ over the short range used, but errors were random from segment to segment so no large-scale metrology error could accumulate. Thus the proportional width error is limited to no more than about $10\mu\text{m}$ which our analysis shows contributes less than 1×10^{-13} to contrast. (For the case of proportional width error, the global allocation is larger than the random one.)

In-plane petal bending in the TDEM petal is negligible. Even with a 250 μm bend from base to tip, the scatter increase is $< 1 \times 10^{-16}$ at the most sensitive wavelength (550nm). The as-built TDEM petal has significantly less bend than this, although it appears to be closer to an ‘S’-shape than a quadratic bend. We will model the ‘S’-deformation in the future but we do not expect it to degrade the performance. While we did not test out-of-plane flatness on the TDEM petal, we did visually evaluate it on the proof-of-concept petal (a 6 m petal of the same construction as the

³“Tip Clip” refers to the very ends of each petal being clipped off by a certain amount.

Perturbation	Amplitude (1σ)	Contrast	Wavelength (nm)
Segment δx	20 μm	5.3×10^{-13}	550
Segment δy	20 μm	6.6×10^{-12}	550
Segment In Plane Tilt	20 μrad	1.6×10^{-12}	550
Segment Placement Total		8.8×10^{-12}	550
1 cycle/segment	15 μm	1×10^{-11}	300
2 cycle/segment	15 μm	7.7×10^{-13}	300
3 cycle/segment	10 μm	2×10^{-13}	250
4 cycle/segment	10 μm	8.1×10^{-14}	250
5 cycle/segment	10 μm	4.4×10^{-14}	250
6 cycle/segment	10 μm	2.8×10^{-14}	250
Segment Shape Total		1.1×10^{-11}	250
Proportional Width	5×10^{-6}	7×10^{-14}	550
Tip Clip	1 mm	1.15×10^{-13}	250
Quadratic Out-of-Plane Bend	5 mm	6.3×10^{-15}	550
Quadratic in-Plane Bend	250 μm	9.5×10^{-17}	550
Non-Segment Manufacture		1.3×10^{-13}	550
Random Error Total		1.5×10^{-11}	550

TABLE 2. Worst-case allocated errors to each of the top 13 perturbations from Table 1 to meet the total allocated contrast due to random petal errors of 1.5×10^{-11} . All errors are 1σ based on an assumed Gaussian distribution among all segments. Global errors contribute less than 30% of the total contrast due to the nominal contrast plus all manufacturing errors.

TDEM petal, but without optical edges) and found the deployed ribs maintained petal flatness to better than ~ 5 mm, leading to less than 10^{-14} increase in scatter.

Our original goal was to create a petal whose manufacturing errors led to less than 3×10^{-10} contrast. This value was selected to be a fraction of a conservative and relaxed overall starshade performance requirement of 1×10^{-9} contrast allocated to manufacturing errors. We also specified the milestone based on the most conservative assumption of identical (global) errors on each of the 30 petals. Even with this conservatism, as we'll show below, our resulting petal achieved a 30% better contrast than the milestone when assuming all errors are global (see Section 7.1).

As we explained at the beginning of the section, however, our experience in manufacturing and measuring the petal shows that we are dominated by random manufacturing errors rather than global systematics. Our results analyzing the measured shape of the occulter also show that our as-built petal shape errors, when considered as random errors on each petal, correspond to an overall contrast closer to a flight starshade designed for 10^{-10} rather than the relaxed 10^{-9} of the milestone (see Section 7.2). We thus have updated our error budget to correspond to this lower flight-like occulter contrast with an allocated contrast to random petal manufacturing errors of 1.5×10^{-11} . Table 2 shows one allocation of errors to the dominant terms in Table 1 that meets this allocation at the worst case wavelengths. Because the contrast is dominated by the random petal-to-petal errors (the global errors contribute roughly 30% of the total residual contrast at the worst case wavelength) we only include the allocation to random errors here for brevity. Including an allocation for the global errors (dominated by the low frequency, 1 cycle/segment error on each segment) and the nominal contrast (roughly 7×10^{-13}) results in a total allocated contrast for manufacturing of 2×10^{-11} . Appendix D shows the complete allocation table for each wavelength including both random and global errors. In Section 7.2 we compare our measured petal against this budget and show that we are mostly meeting even these more stringent requirements.

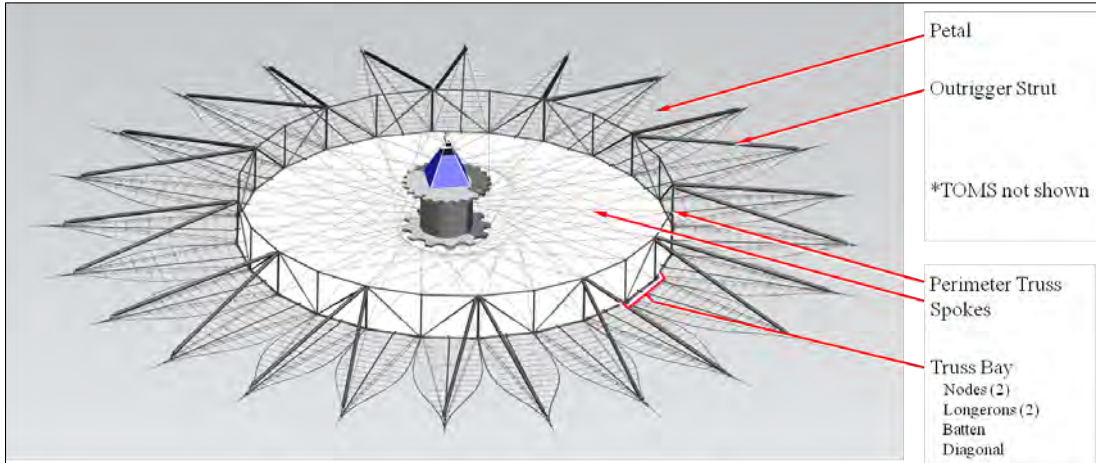


FIGURE 2. Deployed starshade.

4.3. Mechanical Design Summary. The whitepaper describes the mechanical design of the occulter and occulter petal in some detail; we only summarize here for completeness. A schematic of the deployed star shade is shown in Figure 2. The petals are arrayed around the circumference of a deployable perimeter truss (derived from the AstroMesh reflector antenna developed by Northrop Grumman Aerospace Systems (NGAS)). The petals employ a highly mass efficient lattice structure comprised of pultruded graphite fiber reinforced plastic (GFRP) rods that have finely tuned CTEs to limit thermal deformations. The lattice structure is configured and optimized to provide stiffness and stability as required to meet petal stability requirements. When stowed, the starshade petals are wrapped around a fixed, lightweight central hub structure. The hub is sized to provide sufficient annular radius between its outer diameter (OD) and the fairing inner diameter (ID) to contain the stowed starshade truss and petals while maximizing hub diameter to reduce petal strain. The TDEM petal is designed to work with a 3m diameter hub. The petals wrap approximately 2/3 of the way around the hub circumferentially and overlap about 2/3 of the total stowed truss height vertically.

Figure 3 details the petal structural design, as viewed from the telescope (anti-sun) side, with the Thermo-Optical Micrometeorite Shield (TOMS) blanket removed. The primary petal structure is a lattice of battens and longerons that intersect a longitudinal spine and a pair of structural edges on each side. These elements are optimized to place and precisely maintain the optical edge with the required profile tolerance regardless of thermal extremes or structural loads from the relatively thermally unstable TOMS. The lattice is highly mass efficient yet very stiff in-plane. Secondary petal structure includes a pair of deployable ribs in an “A” frame configuration that stiffen and maintain overall deployed petal flatness. The deployable ribs fold outward and flat against the petal when stowed then pop up into place when the petal is unfurling. The ribs are deployed by extension springs that are inside hollow soda-straw size GFRP struts that lock the ribs in place at a near-perpendicular angle to the petal when deployed. The ends of the deployable ribs coincide with truss-to-petal interface nodes on the base spine and with the outboard end of the outrigger at the apex of the “A” to complete the tripod-like geometry of the petal and outrigger support structure on the edge of the perimeter truss. Because we had hoped to find the resources to perform a stow-and-deploy test of the petal we manufactured ribs for the TDEM petal. These were not installed, however, for the metrology tests and resources were not available to perform the deployment.

The battens define and maintain the precise petal edge-to-edge width. They are made from a pultruded GFRP base material that has an axial CTE of better than $-0.2 \times 10^{-6}/^{\circ}\text{C}$ over a

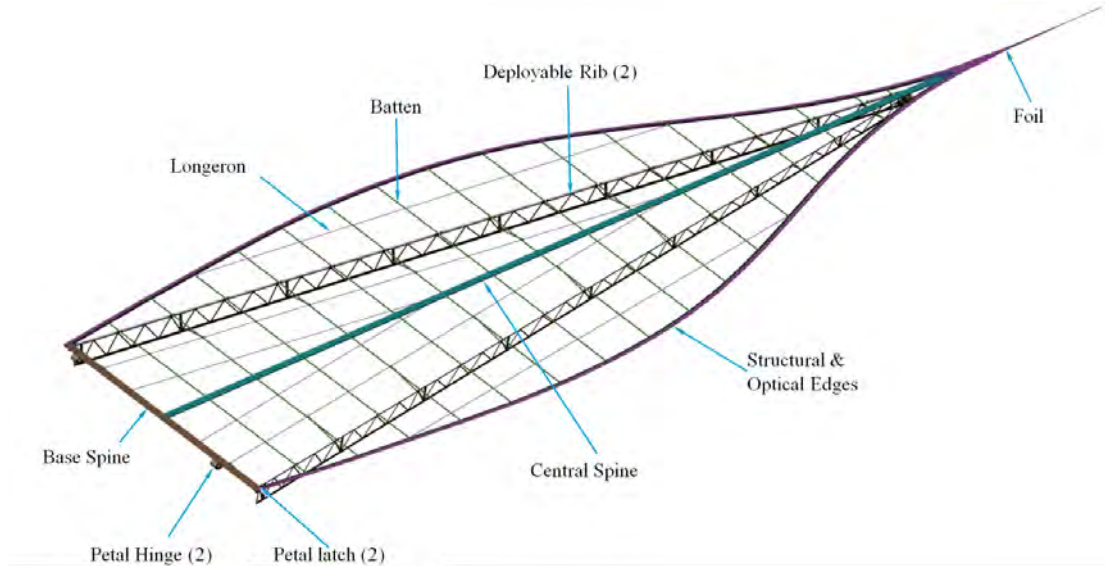


FIGURE 3. Petal mechanical design.

worst-case temperature range of $\pm 100^\circ\text{C}$. The battens are continuous across the width of the petal so that joints will not affect their axial stability. Longerons provide the petal with in-plane shear stiffness for maintenance of the overall shape, though this is limited by the long aspect ratio of the petal. They are made from the same pultruded GFRP as the battens, have a circular cross section and are also continuous along their length. The longest pair of longerons also act as hinge pins for the deployable ribs. Like the battens, the number and placement of longerons is somewhat arbitrary. The longitudinal and base spines provide additional stiffness and are constructed of a foam core sandwiched between thin graphite face sheets. The base spine closes out the petal root structure and carries the perimeter truss interfaces: two hinge points for the unfurling portion of deployment and two precise latches that position the deployed petal in-plane.

All petal structures are designed so that no component is subjected to more than 0.5% strain (5000 μstrain) when stowed around the 3m diameter hub, ensuring that permanent plastic deformation or material creep that would degrade the deployed shape or figure of the starshade will not occur. The maximum strain is only approached in the longitudinal spine and our current design shows a maximum of only 0.2%, a 150% margin. The spine also has little or no role in the definition of the deployed petal edge profile. Its primary function is to accommodate launch restraints and deployment hardware and as a ground-handling interface. The battens are perpendicular to the direction of stowed petal strain and thus will not experience permanent set from material creep prior to launch. Section 8 and Appendix C describe the results of material coupon testing at these levels of strain.

The 25mm wide and 0.4mm thick graphite composite optical edges are manufactured separately from the petal in the longest lengths practical for maintaining the required figure profile; between 0.8m and 1.3m long. The segments are aligned using the FARO arm and then secured with precision clamps for a room temperature cure bonding process. The petal tip is bolted into a transition plate that connects the central spine and edges together. Section 5 describes the manufacture and assembly process used.

5. AS-BUILT PETAL MANUFACTURE AND ASSEMBLY

In this section we describe the manufacture and assembly process of the TDEM petal.

5.1. Material Selection. Most petal components are constructed of carbon composite materials for the sake of mass efficiency and stability. Exceptions include the spine foam cores, assembly parts and hinges.

Battens are commercially available hollow carbon pultruded rods made of Toho IMS60 E13 fibers and premium grade bisphenol epoxy vinyl ester resin and of 0.25in square section. The longerons are also solid pultruded rods but are made of Toray T-700 S fibers with the same premium grade bisphenol epoxy vinyl ester resin. They are .125in round cross section. The tested CTE over the temperature range of interest is 0.2 ppm/°C, which is adequate for this application, but can be reduced further by optimizing the fiber via choice of resin types and ratios. The pultrusion process yields unidirectional fibers with a precisely controlled resin volume ratio, for uniform and controllable CTE performance.

Structural edges are machined from a high-modulus quasi-isotropic GFRP carbon composite laminate using Toray M55J fibers and Patz Materials and Technologies PMT-F6 cyanate-ester resin in a [60/-60/-60/60/0/0/60/-60/-60/60/0/symmetric] laminate with 0.0045in thick plys. They are thus approximately 0.10in thick and 1.2in wide. The deployable ribs are machined from this same laminate although they were not installed in the TDEM petal during the current phase of the project.

Optical edges are made from a GFRP laminate similar to the structural edges, but have 0.003in thick plys in a [60/-60/0/0/-60/60] laminate resulting in a much thinner (0.018in thick) material. The fiber orientation in the manufactured optical edges is critical to avoid the possibility of having any fiber direction being close to parallel (or tangent) to the overall in-plane profile of the optical edge profile, i.e. we cut “across the grain”. This makes it possible for the shape of the optical edge to be maintained to the highest possible degree both during manufacture and upon handling and long-term use. Strands of parallel/tangent fibers on the 25-50 micron radius cross-sectional profile would otherwise be easily shed due to minute stress risers between fibers and resin. On average, the fibers are oriented perpendicular to and ± 30 degrees from the nominal cut direction, noting that the edges are curved in shape.

The spine face sheet ply thickness and sequence of fiber orientations are identical to the optical edges. The fiber orientation in the manufactured spine face sheet parts, however, is rotated 90 degrees to allow the laminate zero-degree fibers to be parallel to the parts, which is desirable in this case.

5.2. Manufacturing Process. The battens and longerons were purchased from Diversified Composites in Erlanger Kentucky in special runs to produce very long, straight pieces. They were cut to length and then the battens were machined using a computer numerical control (CNC) router for the slots and holes that the structural edges and longerons are bonded into. The other parts were machined from large sheets of GFRP. JPL provided the M-55J fibers from excess Flight materials and Patz Materials and Technologies prepared two different resin impregnated tapes (pre-preg). A second company performed the layup and curing (Applied Aerospace Structures Coporation, AASC) and a third company performed the machining (Roncelli Plastics).

The structural edges, ribs and spine face-sheets were machined with a conventional CNC router using phenolic sandwich tooling for reinforcement of the thin materials. Machining of the optical edges is the key issue here and three different technologies/vendors were evaluated by AASC as this task was a part of their contract. Each vendor was sent an early test sheet of GFRP and asked to machine 3 optical edges per a provided computer aided design (CAD) model of 1 edge of representative profile but approximately half the length of the intended design. The half-length was decided upon to accommodate one of the vendors, which could not process a larger part with currently available equipment. The three machining technologies and companies were: 1) conventional CNC router (Roncelli Plastics), 2) water jet cutting (Micro Water-Jet Cutting) and 3) micro abrasive blast milling (IKONICS). These machining vendors were not funded for the test

cuts and were limited to companies that AASC had an established working relationship with. These technologies are by no means considered comprehensive. Notably missing are grinding processes such as conventional creep-feed and those used for precision optics.

The demonstration edges were evaluated primarily as to the apparent integrity or “cleanliness” of the cut. However, the results were not considered conclusive, as in all cases further processing was needed, as is typical for creating sharp edges, such as the honing of cutting edges. Also, the method for holding down the very thin and light-weight parts is critical and the vendors were not given the time nor funding to develop an optimal technique. The selection was made based on more practical matters, such as the size of part that could be processed, schedule performance, and proximity to JPL. Roncelli Plastics was the vendor selected for machining all parts, using conventional CNC router machines.

Experiments were performed to determine if a beveled edge with the desired radius of curvature could be machined with a router. This effort was not successful and abandoned due to cost and schedule constraints. A decision was made to proceed with optical edges with square cuts and defer development of beveled edges.⁴

Additional experiments were performed to determine optimal cutters, cutter speed, feed-rates, feed direction and hold-down methods. The selected hold-down method was to sandwich the GFRP sheet between 2 thick sheets of phenolic plastic bolted together and bolted to the router table. The parts were lightly sanded to remove burs at the top and bottom faces but care was taken not to touch the middle layers, which define the edge profile.

The petal structure was assembled starting with the base spine and then positioning the battens and bonding them to one face of the central spine. Foam core was then added to the central spine in between the battens and then the second face sheet was bonded to the central spine. The structural edges were installed next, followed by the longerons. The optical edges were designed to extend over the structural edges by 0.25 in. The installation and metrology of the optical edges is described next.

5.3. Optical Edge Metrology and Installation.

5.3.1. *Installation Plan.* The optical edge on each side is divided into 5 segments about 40in long (an additional piece would form the tip) for ease of handling and installation. A FARO Advantage Platinum, 8ft reach portable measurement arm was used to position the optical edges onto the mechanical edge. The FARO has a reach of approximately 96in side-to-side and therefore is capable of measuring across the entire width of the petal. However, the FARO has a limited accuracy of about 30 micron per meter (see Table 3). Since it was desired to set the edges to 10 micron accuracy, a system of calibrated buttons on the optical and structural edge was developed. This limited the use of the FARO to short range where an accuracy of approximately 8 microns could be achieved. Each piece of the optical edge thus has five “buttons” installed into holes evenly spaced along its length starting approximately 1 in from either end. The buttons consist of a conical hole drilled into a flanged part that is glued into the edge section to form a set of fiducial positions. A second set of buttons is set into the mechanical edge, two on either side of each batten. With the distance between battens being approximately 10in, the optical edges are set with ends adjacent to a batten. This results in four sets of buttons on the mechanical edge per optical edge section, and five sets on the optical edge itself. This meant that when using the fiducials to fit the edges, measurements between fiducials were shortest at the ends of the optical edge. Buttons placed near to the ends of the optical edge segment and near to the batten ends would be only 1in or so apart, enabling the FARO’s best accuracy to be achieved at these locations.

⁴A development program for beveled edges is now underway at Vanguard Space Technologies, Inc under their NASA SBIR 2011 Solicitation Award for which JPL is the technical monitor: PROPOSAL NUMBER: 11-1 S2.03-9736, SUBTOPIC TITLE: Precision Deployable Optical Structures and Metrology, PROPOSAL TITLE: Fabrication and Measurement of Precision Structures for External Occulter Optical Edges at Vanguard.

	Allied	Hexagon	FARO
Linearity			
x-axis	21 μm (5 m range)		16 $\mu\text{m}/\text{m}$
y-axis	8 μm (2.5 m range)	1.24 $\pm 0.1 \mu\text{m}/\text{m}$	
z-axis	4 μm (1.6 m range)		
Repeatability			
x-axis	3 μm	1.4 μm	32 μm
y-axis	5 μm	0.7 μm	34 μm
z-axis	4 μm	0.9 μm	11 μm

TABLE 3. Measurement machine calibration summary data for Allied, Hexagon CMMs and FARO arm. Repeatability is the total range of measurements to a fixed point over repeated trials (encompassing both biases and random error). Since the different testing agencies used different test protocols, the data are not directly comparable, but serve as a guide to performance. The Allied linearity numbers represent the maximum deviations expected at the maximum range of the machine (which can be translated into an error in slope). Hexagon calibration data was only provided for the y -axis direction and represents a roughly 1σ slope error. Likewise, the FARO slope error is only provided as a radial specification. External calibration and certification was done on the Hexagon machine on 5/2/2011, the Allied machine on 8/22/2011 and the FARO on 3/29/2007. Copies of the certification data are available on request.

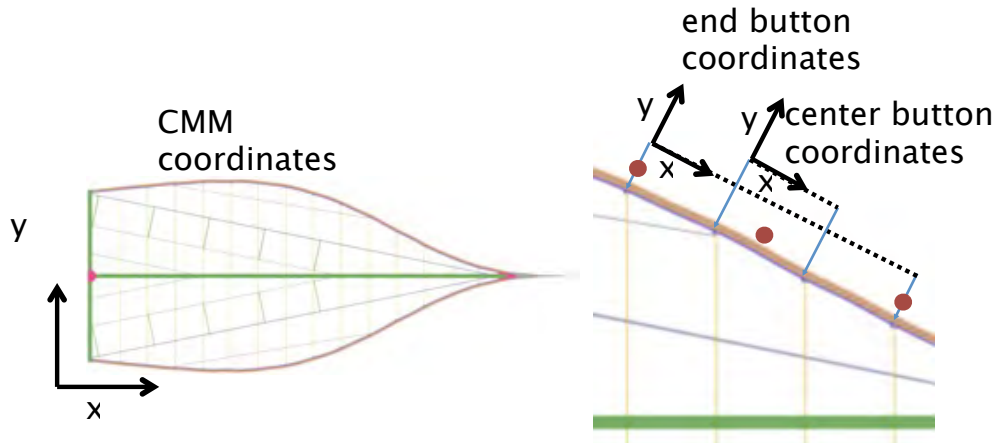


FIGURE 4. A schematic of the global and local coordinate systems used for optical edge placement.

All structural button positions are defined relative to a global coordinate system with origin at the center of the full occulter, and the x -axis passing through the center of the petal. (Selecting this coordinate system allowed the edge shape, as designed by optimization, to be aligned with respect to the buttons without translation or rotation.) In addition, each pair of buttons on the mechanical edge is used to define a local coordinate system with origin at one of the buttons, x -axis toward the next pair of buttons and y -axis perpendicular. The FARO is used independently in each local coordinate system for optical edge placement to ensure that it is only used over short ranges. The global and local coordinate system is schematically shown in Figure 4. To properly calibrate

the short range use of the FARO, independent measurements of each button location in the global coordinate system was necessary.

Measurements of the locations of the structure buttons prior to the assembly of the petal were made at Allied Mechanical in August 2011 using their DEA model Delta SP 512518 CMM machine. Because the table under the CMM machine was too small for the whole petal, a system of outriggers was placed on the table to support the outer edges. Table 3 shows calibration accuracies for the three coordinate measuring machines used in the project. Four sets of measurements were taken at Allied, but one was incomplete and was not subsequently used. Data was received in a PC-DMIS format, and run through a custom parser to extract Cartesian data points. These data points were aligned with the global coordinate system and the three data points for each button were median-combined to drop any outliers. The resulting median Allied measured location was used as the “truth standard” for the location of each structure button. All subsequent placement would be done with respect to these button locations. Repeatability of the measurements was within the expected $5\mu\text{m}$ as in Table 3.

An interactive graphic user interface (GUI) was developed to provide segment button locations relative to a coordinate system centered about any pair of structure buttons, which allowed the coordinate system to be quickly shifted from segment to segment; a typical view of it is shown in Figure 5. Three buttons are selected at a time to serve special functions: the origin is shown in green, the direction of the x-axis is in magenta, and the button whose coordinates are being defined is in red; Figure 6 shows a close-up of these buttons, placed on segment 7 as an example, with the axes of the local coordinate system shown for clarity. A new button can be selected by clicking it; shift-clicking and ctrl-clicking redefines the origin and axis, respectively, and double-clicking resets the GUI. The coordinates of the selected button are given in the title.

5.3.2. Measurement of segment edges. In order to accurately place each segment, measurements were needed of the optical edge buttons relative to the actual segment edge. (See Figure 7 for a diagram and the segment numbering.) These measurements also provided an estimate of the Roncelli manufacturing error and an early indication of whether the edges were meeting the requirements for the desired contrast. For these measurements, the edge sections were taken to Hexagon Inc. (Lake Forest, CA) and placed on a large CMM machine, type Global Advantage 122210. This machine uses digital camera techniques coupled with a precision rail system to make measurements. Its advertised accuracy is listed in Table 3. To perform the Hexagon measurements, optical edge segments were placed onto the measurement table over a white paper background. This gave adequate contrast to the black edge for the measurement software. Two sets of measurements were made: the edge shape was measured at $\sim 30\mu\text{m}$ increments along the edge relative to the origin of the CMM and the positions of each button were measured, both with the optical camera in the same coordinate system.

To align each segment in the global coordinate system, the Hexagon edge data was fit directly to the designed edge. As it is generally not possible to assign a measured point exactly to a corresponding point on the ideal profile, this fit was done by heavily oversampling the designed occulter edge with respect to the Hexagon data, storing it in a KD-tree, and minimizing the nearest-neighbor distance from each Hexagon point to the designed edge with a nonlinear least-squares algorithm. (A k-dimensional tree, or KD-tree, is a structure for storing multidimensional data, such as sets of points. Like other types of tree structures, it consists of a single root node which links to a set of daughter nodes, which in turn act as the root node for their own daughter nodes, and so on recursively until no subtrees remain. In the case of a KD-tree, the root node contains a bounding box which is large enough to encompass every point in the data set. The daughters each contain a partition of that box along one dimension, chosen such that each subdivision contains half of the data points (or possibly one less, should there be an odd number of data points). This partitioning continues, cycling through each coordinate, until every terminal node contains a

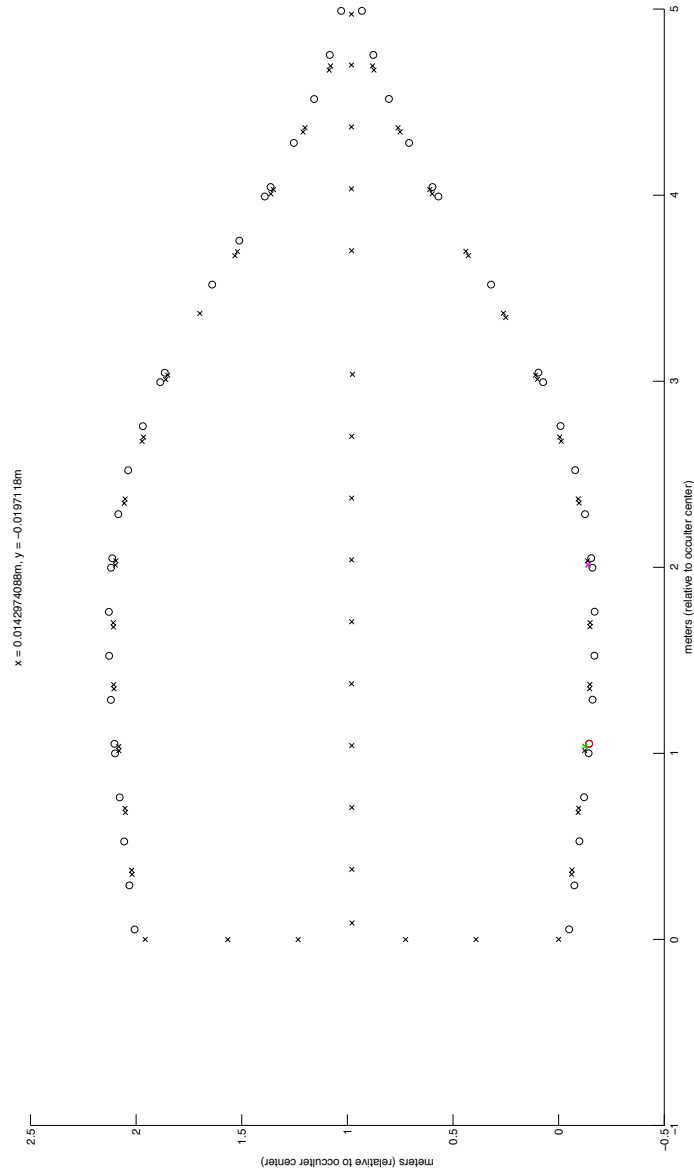


FIGURE 5. A sample configuration from the placement graphic user interface (GUI), showing the positions of all buttons which can be used with the FARO arm. x's are buttons on the structural edge and o's are buttons on the optical edge.

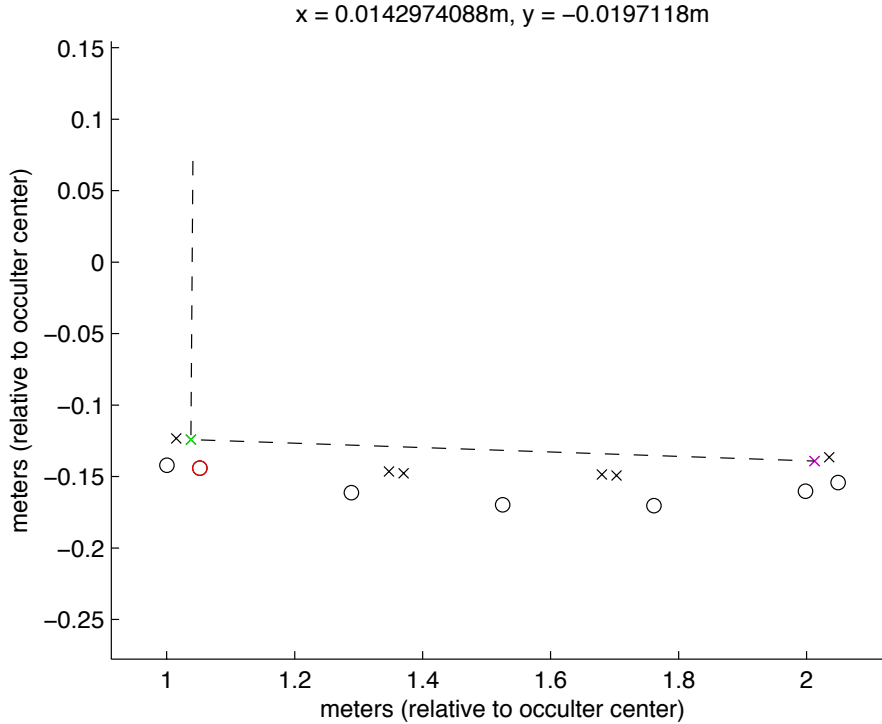


FIGURE 6. A zoomed-in version of Figure 5, showing a close-up of the buttons in the vicinity of segment 7. Local coordinate x - and y -axes have been added as dashed lines for clarity. Three buttons are selected at a time to serve special functions: the origin is shown in green, the direction of the x -axis is in magenta, and the button whose coordinates are being defined is in red.

single point. The primary advantage in using KD-trees for nearest-neighbor searching is that by partitioning the tree by location in space, it becomes very quick to exclude entire subtrees which cannot be the nearest point.) A KD-tree is an ideal data structure for this application, for while it takes $N \log N$ time to initialize, searches for nearest-neighbor points can be done in $\log N$ time, and the KD-tree itself can be saved and used repeatedly.[7] This fitting approach was also used in all subsequent incidences when two sets of points were required to be aligned.

The residuals from these fits can be seen in Figure 8. These plots show that the measured performance was quite a bit worse than the small quoted errors in Table 3. Hexagon’s quoted measurements assume pure two-dimensional targets. Because the optical edges have a significant thickness, the exact position of the edge was obscured by partial shadowing. The software’s ability to define the edge based on dark contrast against the white background was thus limited by the three-dimensional appearance of the top of the edge. The results was a much noisier measurement than expected with occasional large outliers or “spikes”. The resulting error was roughly $10 \mu\text{m}$ rms with maximum deviations of roughly 30 to 40 microns, close to 50 times the quoted repeatability.

Nevertheless, the noise is still below the rms shape error requirement, and the large number of measurement points allowed us to easily filter the high frequency noise. Figure 9 shows the same residuals but low-pass filtered to reduce the noise. Both figures show that while the ideal edge profile tracked the manufactured edges well, four of the segments (1, 3, 6, and 8) were determined to have significant overall bends. The largest, on segment 8, reached $200 \mu\text{m}$ peak-to-valley, and would have consumed the entire error budget for the petal; the desired locations of the edge buttons on these segments were adjusted such that these bends would be compensated for when the edge

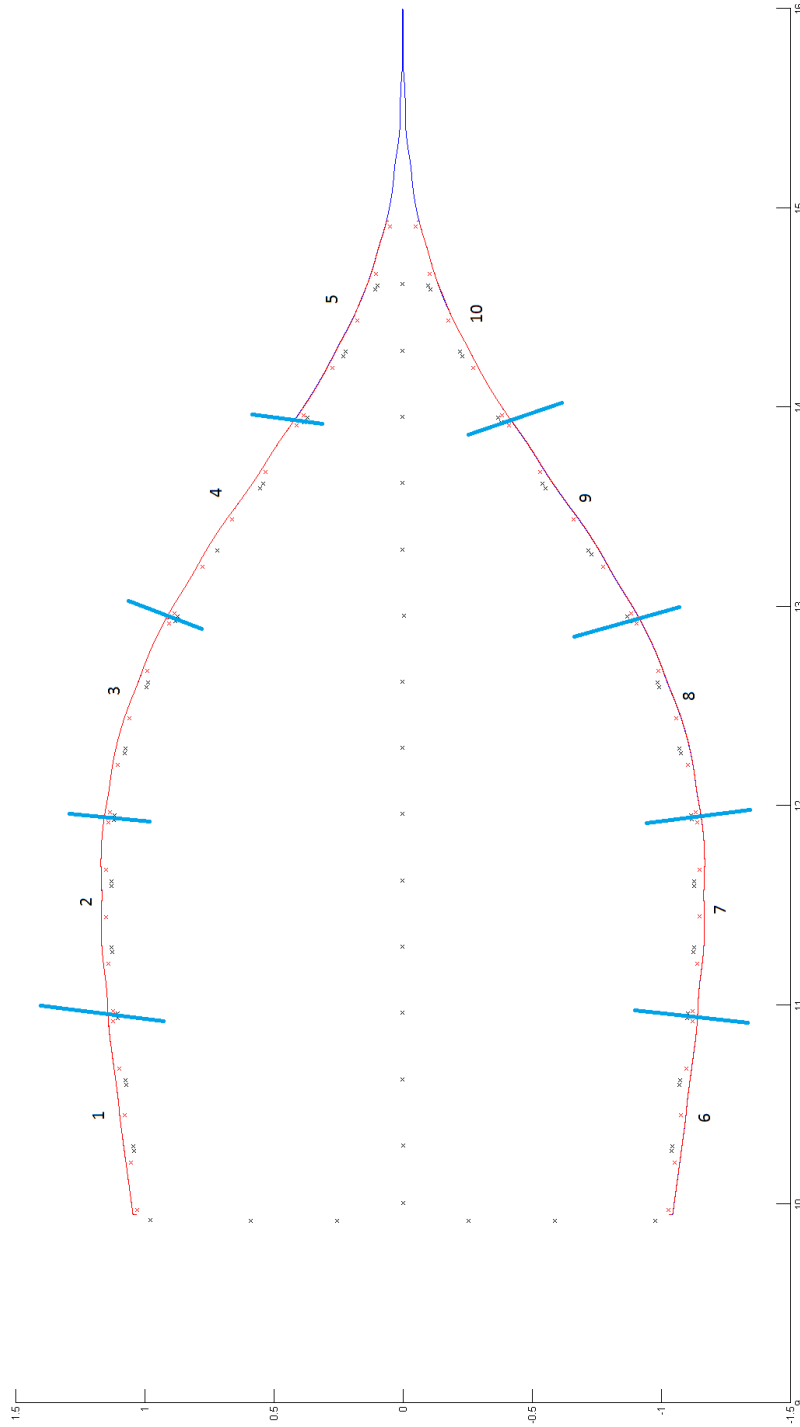


FIGURE 7. The locations of the 10 segments on the petal, along with all buttons marked by \times on the structure (black) and on the optical edge (red). The segments as measured by Hexagon metrology are shown as red lines, and the optimal design shape is shown in blue (not visible at this scale).

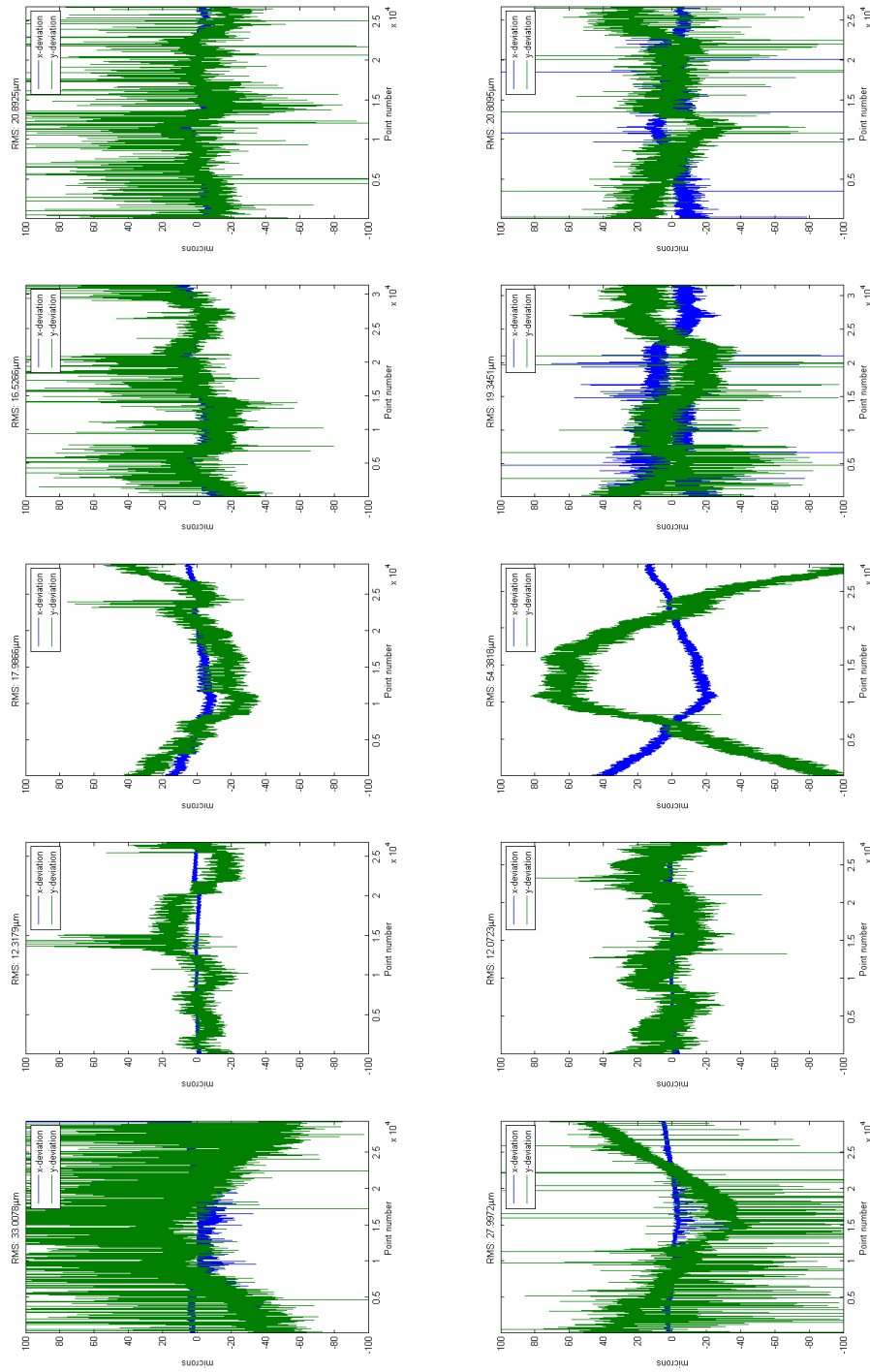


FIGURE 8. A comparison of the residuals from fitting the measured Hexagon shapes to the designed edge. Blue and green curves are nearest-neighbor x- and y-differences, respectively, between the Hexagon data and a finely-sampled version of the ideal profile in a coordinate system with the x-axis aligned to the central spine of the occulter. The sample points of the ideal profile are chosen to minimize the L2-norm of the vector of total distances [i.e. $\sqrt{x^2 + y^2}$] from each Hexagon data point. Segments 1-5 run across the top row, and segments 6-10 across the bottom. RMS error for each segment is given at the top of each subplot. Significant bends are visible in segments 1, 3, 6 and 8.

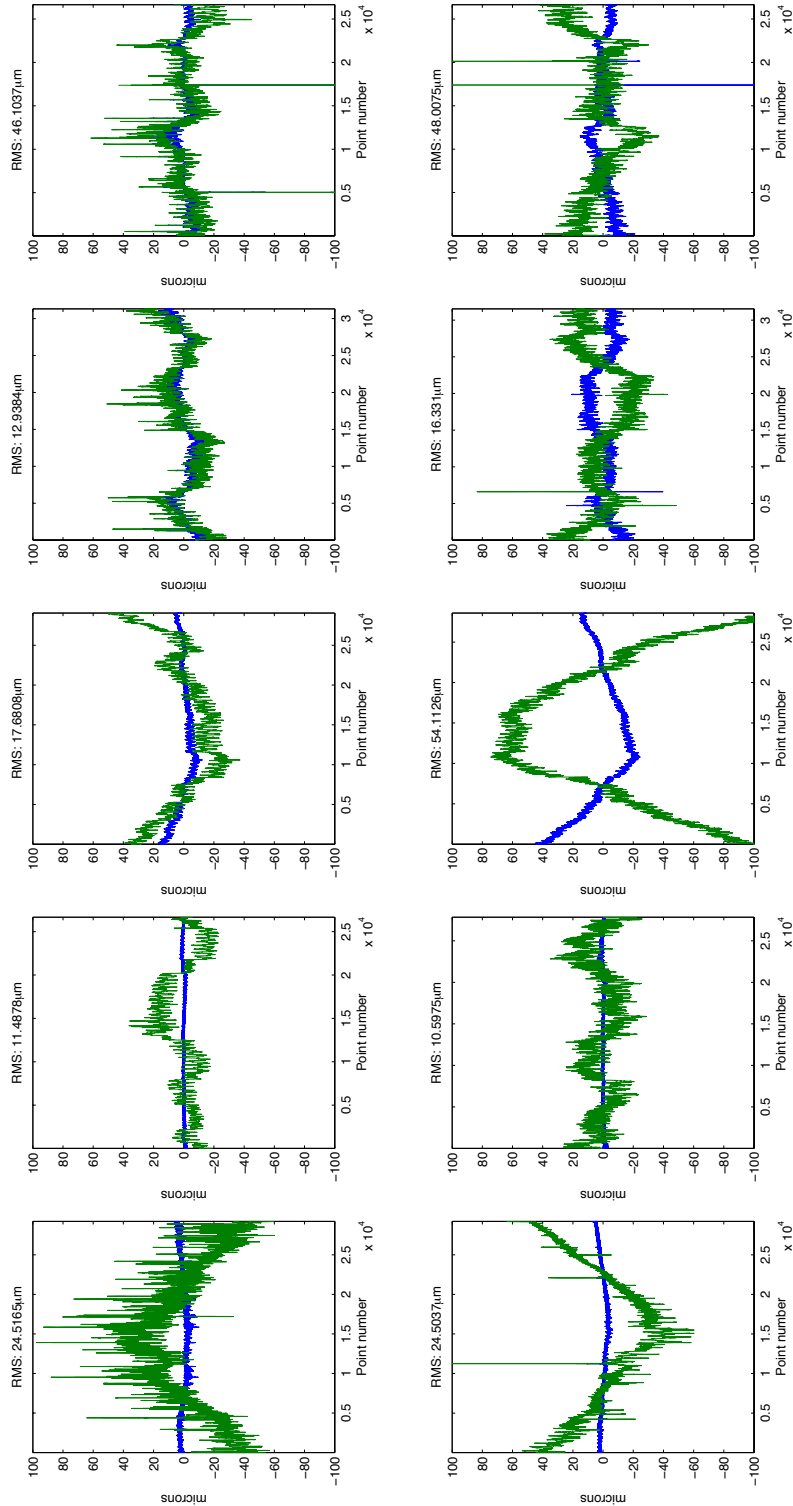


FIGURE 9. A comparison of the residuals from fitting the measured Hexagon shapes to the designed edge after low pass filtering the measurements. Blue and green curves are nearest-neighbor x- and y-differences, respectively, between the Hexagon data and a finely-sampled version of the ideal profile in a coordinate system with the x-axis aligned to the central spine of the occulter. Segments 1-5 run across the top row, and segments 6-10 across the bottom. RMS error for each segment is given at the top of each subplot. Significant bends are visible in segments 1, 3, 6 and 8.



FIGURE 10. Setup of an optical edge for measurement with the FARO arm. Additional weights (not present) were also placed between the fixed clamps. The orange pieces are the low-friction surface and the white pieces are the height shims for the edge.

was assembled. Some small adjustments in desired button location were made manually as well to shift the segments along their long axis, to avoid the segments overlapping. All of these changes were propagated through to the button locations on the segments, which reduced the problem of placing the edge to one of correctly placing the buttons with respect to the Allied “truth standard”.

Fits to the Hexagon data (both before and after low pass filtering) were also used to estimate the contrast to confirm that the as-cut edges were meeting the milestone requirement. These fits included 3 polynomial terms to account for the bends in segments 1, 3, 6 and 8. A simulated occulter was created with 30 identical petals assuming all the as-measured edges were placed perfectly during installation. The resulting contrast ranged from 1.2×10^{-11} at the best wavelength to 6×10^{-11} at the worst-case wavelength. This gave us confidence that the manufacturing of the edges was sufficient. A more detailed description of the modeling and analysis can be found in Kasdin et al. 2011.[8]

Unfortunately, using the Hexagon CMM to locate the edge buttons relative to the optical edge was problematic as the cone feature was not particularly distinct under the camera and lighting. The resulting button-edge distances after differencing were inconsistent with direct measurements of this distance with the FARO arm at levels up to $200\mu\text{m}$ in some cases. To compensate for this, five sections of each edge located adjacent to buttons were measured with the FARO arm directly; the combined set of 5 were fit to the Hexagon edge data on each segment to place the buttons relative to the edge. A plastic sheet was placed onto the optical table to provide a low-friction surface. Edge segments were placed onto 0.050 shims to space them up from the surface by 1.5 mm and secured using clamps near every button location, see Figure 10. Small magnetic weights were also placed on the edge to hold it down uniformly. This process was done carefully to avoid bending or deforming the edge section. The shim thickness was chosen to bring the ball centerline of the FARO probe up to the center of the edge when the ball was touching the table as shown in Figure 11.

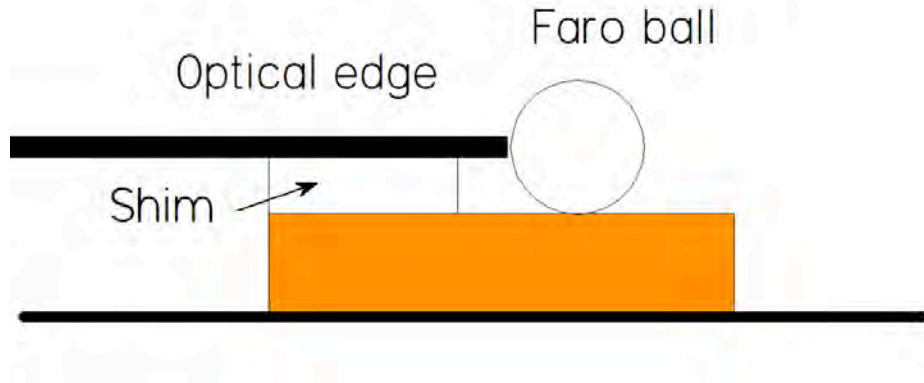


FIGURE 11. FARO ball stylus shimmed to measure the boundary of the optical edge.

A baseline for the measurements was established using the first and last button of the edge piece and then a series of measurements was made near each button, extending approximately over a 2in length. In addition, all the button locations were measured. The sets of data were processed to yield the location of each button center relative to the optical edge. The final transformation was then applied to bring the FARO button measurements into the global frame.

Two complete sets of Faro data for the 10 edges are available. These were used to calculate the distances to the edge from the buttons. The difference between the two sets for these distances was then calculated and the resulting set of data has a mean of 0.2 micron and standard deviation of 7.9 micron, consistent with the 8 micron error quoted for the Faro measurements over a short distance. Systematic errors originating within the Faro arm would not be captured by this, and so in a calibration exercise, the arm was used to measure a set of gauge blocks. The mean difference between the calibrated sizes of a set of gauge blocks around 25 mm in thickness and the sizes measured by the Faro arm was -1.9 microns, indicating a very low offset within the Faro arm.

5.3.3. Optical edge installation. The petal was placed on aluminum extrusion pieces secured to a large table consisting of two optical tables securely joined together. At the widest part of the petal, the tables had aluminum extension pieces attached to accommodate the full width. Owing to slight waviness of the petal, the extrusion pieces (of various lengths) were shimmed where necessary to provide good contact with the petal.

Since the table would expand and contract as the temperature in the room varied, while the petal, having a low CTE, would not, the petal was secured to the table only in two places near to the current site of activity. The petal was secured on a batten in one place near the FARO's base (bolted to the table) and in another near to the edge. This ensured that the petal remained fixed relative to the FARO arm but would be free to slide on the table so that potential thermally-induced distortions would be minimized.

Having secured the FARO and the petal, a baseline was set up for the FARO, normally consisting of the two batten-end buttons which would be nearest to the optical edge ends, and a third point, normally on the base spine, to define the measurement plane. At the ends of the petal where the distribution of buttons was different, the nearest available structural buttons were used.

Now the optical edge was placed onto the structure and manually positioned to within 1 mm of its eventual location. A rule was placed along the line between the endmost structural buttons of the section and three linear translation stages positioned so that they would translate in a direction perpendicular to the line. After securing a stage to the table, a thin shim was placed to cross between the stage and the optical edge. Two small spots of cyanoacrylate adhesive were used to secure the shim to the optical edge. A bolt and washer secured the other end of the shim to the

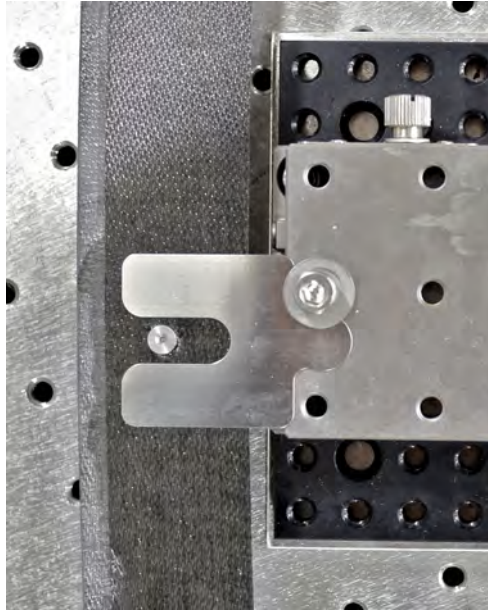


FIGURE 12. Detail of stage and shim attachment to edge piece.

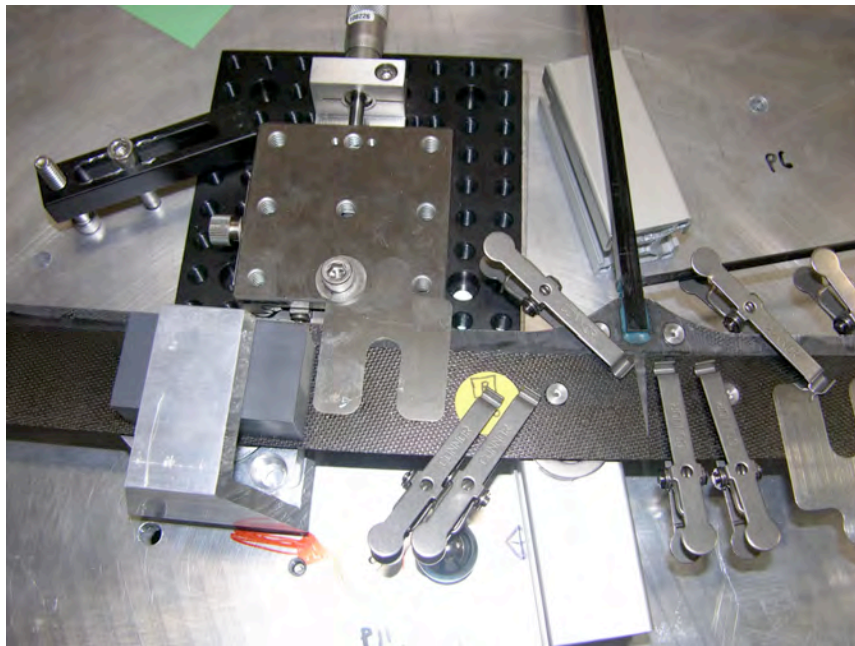


FIGURE 13. End of edge section showing translation stage and shim attachment used to adjust edge. Also shown are the metal clips and left, the aluminum and grey plastic spacer are part of the pneumatic clamp.

translation stage as shown in Figure 12. This bolt and washer combination could be released and retightened to alleviate strain when the optical edge was repositioned. At one end, the translation stage was a two-axis stage so that the longitudinal as well as the transverse position of the edge could be adjusted.

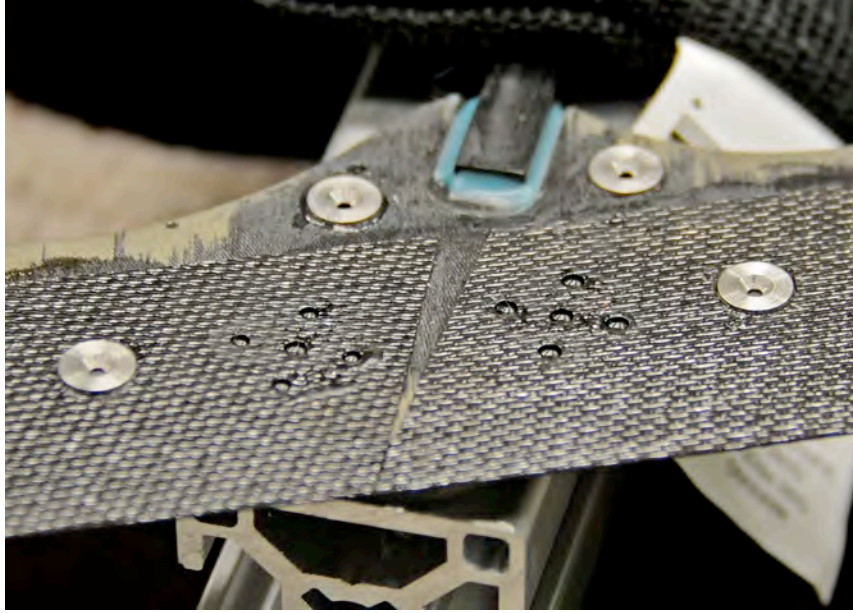


FIGURE 14. Detail of the junction of two edge pieces showing the two batten-end buttons and the two edge piece end buttons. The pattern of five holes is the injection/relief holes for the epoxy bonds.

Next, the FARO ball was placed into the optical edge's end button and the two-axis stage adjusted to bring the button to its correct coordinate. Then the edge was clamped at the button to the structural edge using min-spring clamps shown in Figure 13 (McMaster-Carr type 5015A2). These clamps are 17-7 PH stainless steel with an Inconel X-750 spring and have smooth clamping surfaces to prevent marring. Approximately 10 of the clips were fastened along the edge to ensure strain-free positioning and good contact with the structural edge. By an iterative process of clamping, unclamping and adjustment the two ends were brought to their correct coordinates while producing minimal strain in the edge. The longitudinal position of only the end button nearest the base spine was set; the other end was allowed to float in that direction, producing minimal longitudinal strain.

Once the two end buttons were positioned, pneumatic clamps were activated to firmly fix the ends. Then a third positioning stage was located near the center button and attached to the edge. After rechecking the end button positions to ensure they had not moved, the intermediate clips were removed and the stage was adjusted to bring the transverse position of the center button to the correct coordinate. Once this position was achieved the center button was pneumatically clamped. The repositioning at the center will generally introduce a strain in the edge section, though well below the limiting strain. For example, a 200 micron displacement of the center button would introduce a small strain of only 0.005%. Typically, the adjustments that were made were much smaller than this.

Next, the edge was bonded to the structure in two stages. First, a line of cyanoacrylate adhesive was run along the inboard edge of the optical edge to adhere it to the structural part. This adhesive could be softened using acetone and cut with a knife if removal was later required. Later, after all the edges were in place and the measurements showed satisfactory positioning, the edges were glued using Hysol 9320 epoxy adhesive injected into pits milled into the structural edge to form a permanent strong attachment. Figure 14 shows the finished junction of two edge pieces, the glue points and the button geometry.

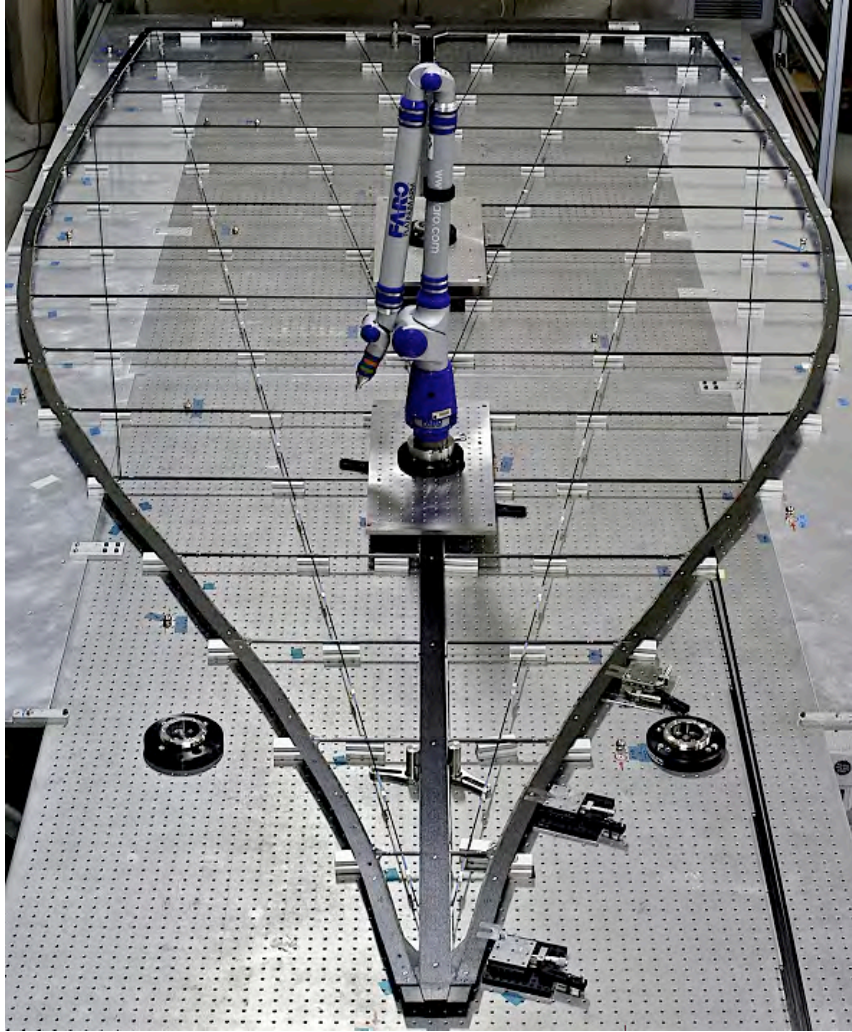


FIGURE 15. Assembled petal on the table at JPL, supported by small sections of aluminum extrusion extending onto the table extensions. The FARO arm is mounted on a bridge over the central spine. Translation stages are in position for adjustment of the right tip-most edge segment.

After completion of the installation of the ten edges, the positions were remeasured and it was decided to remove and reattach the two tip-most pieces. Following this, the measurements were satisfactory and the final bonding was performed. The fully assembled petal is shown in Figure 15.

6. ASSEMBLED PETAL SHAPE METROLOGY

The final assembled petal shape was measured at Allied Mechanical over the 7th and 8th of February, 2012.⁵ These consisted of measurements of the entire optical edge made every centimeter, and of every button (excluding a few of the spine buttons). The petal was set up on two tables which were carefully adjusted to be coplanar, using longer pieces of extrusion as outriggers under the battens where the table width was less than the petal. To insure thermal stability during

⁵Five measurements were taken at Allied. The first two calibration runs were completed at 9:36 pm and 11:06 pm. The three data runs took place between midnight and 5:00 am of the 8th, finishing at 1:31 am, 3:22 am, and 5:12 am.



FIGURE 16. Setup of the petal on the tables at Allied. The black and grey bags are bearing-filled bags that load the petal to maintain contact with the extrusion pieces.



FIGURE 17. Petal assembly dimensions as positioned on the table at Allied.

metrology the tables had been allowed to reach thermal equilibrium before setup. Then the petal was clamped at the center of the base spine and lightly weighted elsewhere so that it would remain flat yet structurally decoupled from the cast-iron tables. Figure 16 shows the petal set up on the table at Allied and Figure 17 shows the physical arrangement of heights, etc.

A slightly different procedure was followed for the button measurements than was used the first time, and a different probe tip was used. A ruby cylindrical probe (Renishaw A-5000-8876, see Figure 18) with a small diameter (1 mm) and a hemispherical end was attached to the CMM. The hemispherical end performs most of the normal functions of a ball probe for measuring surface heights and surfaces inside the buttons. For measurements of the optical edge location, made every 1 cm, the side of the probe was used. If the cylindrical probe is held vertically, it will make a reliable measurement of the extreme edge of the optical edge.

Four points were taken on each button flange, then the probe was dropped inside the button center to take four points inside the cone (illustrated in Figure 19). Then four more points were



FIGURE 18. Cylindrical probe measuring inside the button at Allied. The edge of the cylindrical probe was also used to measure the edge location.

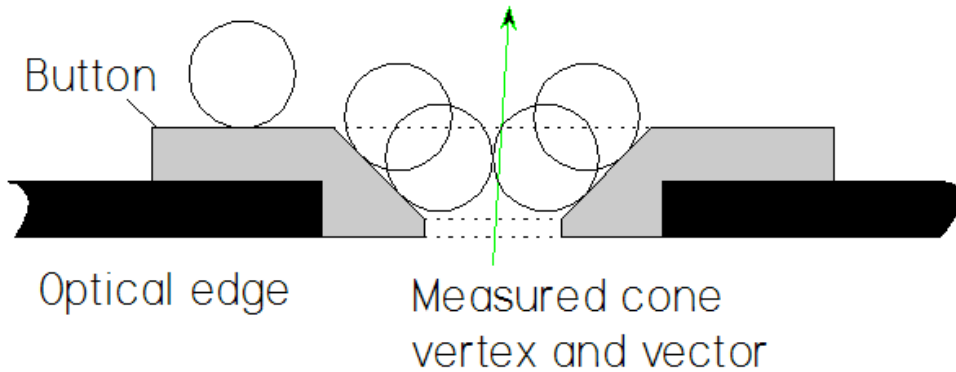


FIGURE 19. An illustration of measurements taken inside and on the button.

measured on the flange in a slightly smaller circle, and the probe dropped further inside the cone to take a second set inside the cone. The two sets of cone measurements would later be used to determine if the cone had been set into the edge at an angle.

Before measuring the width, the edge of the petal was found to have a height variation of up to 1 mm. To ensure an accurate vertical position of the cylindrical probe when set against the optical edge (required to reduce any artifacts of tilt of the cylinder axis), a preliminary set of edge height measurements was made and then entered into the measurement program prior to the edge measurements. This manual procedure took some time. The CMM machine then measured the entire petal, buttons and edges, 5 times. Each time, a baseline was established from two base spine buttons and the longitudinal spines endmost button. Care was taken not to allow the petal to

be touched by anything other than the CMM during the entire process. The measurement data was extracted between each set and compared with the expected differences in x and y between the structure and petal buttons from the previous set of measurements. Immediate analysis of this data showed consistency between data sets and gave a preliminary indication of satisfactory results. Full analyses were made later at JPL and are described in the next section.

7. CONTRAST CALCULATION

In this section we describe how we processed the Allied measurement data to arrive at an estimate of the expected contrast from an occulter made from the as-built petal. There are two sources of statistical variation that contribute to uncertainty, measurement error and manufacturing error. Ideally, in a project such as this one, a statistical confidence in our ability to meet requirements in manufacturing petals would be found by building and measuring many petals. This recognizes that the as-built petal is just a single member of a statistical ensemble of petals encompassing the expected variations in manufacturing. Building and measuring many petals would allow us to average both this manufacturing error and measurement error and come to reasonable estimates of both the mean contrast from an occulter built of similar petals as well as the standard deviation.

Clearly, however, this was not possible within the funding and schedule constraints of the project. Instead, we examine the more conservative success criteria that an occulter built from 30 petals identical to the as-built meets the contrast requirement. This is more conservative as global errors on the petals sum rather than average, producing a higher net contrast. The statistics of the computed contrast are then given only by the error in the edge measurements. We formed an independent estimate of the measurement error distribution based on calibration data supplied by Allied. This process is described in Appendix B. The result, as we explain in Section 7.1 below, was an estimated distribution of contrast for an occulter made up of 30 petals with the best fit edge shape to our as-built and measured petal. This corresponds to the worst-case global error discussed in Section 4.2.

Fortunately, we can also say some things about the distribution underlying the manufacture of the petal. Because we built the optical edge in 10 separate segments, we were able to estimate the manufacturing statistics under reasonable assumptions of the independence of each segment. This allowed us to also calculate the contrast from an occulter populated with 30 different petals with random variations consistent with what we saw in the 10 optical edge segments we built. The result is an estimate of contrast that is more realistic and more consistent with our error budgeting process. We describe this in Section 7.2.

7.1. Milestone Contrast Calculation. As described in Section 6, after assembly the petal was shipped to Allied Mechanical for final measurement of the shape. This included measurement of the locations of both the complete set of buttons and of the edges in 1cm increments, using a cylindrical probe with a hemispherical tip to permit the data to be collected without switching the probe. We processed this raw data by subtracting off the systematic measurement biases discussed in Appendix B for all points, and then fit the measured structure buttons to the “truth standard”—the initial Allied measurement—to align the measured petal in the global coordinate system.

To find the contrast from the petal as built, we used an average of the 5 Allied edge measurement data to simulate a complete starshade of 30 petals by rotating this shape about the origin by $\pi/15$ and replicating it, filling in the mm-scale gap at the truss boundary between the two with a circular arc; this is repeated for all 30 petals, and the shape is closed. As the tip was not built, the shape in this region was taken straight from the design. This closed curve was used as the input to an efficient line-integral-based propagator [9] which does not require analytic representation of errors to evaluate the field downstream.

This approach, integrating directly around the edge, is a significant departure from the proposed contrast-estimation scheme given in the original whitepaper. That approach involved estimating coefficients of a set of known errors in radius, r , from the measured shape on the edges, and inserted the fitted, analytically-defined shapes into a Bessel-function-based propagator [10] to determine the electric field downstream from the occulter. Two factors motivated this change:

- (1) *Improved precision.* The original concept had called for the edge to have its final measurements done with a FARO arm with an estimated $12\mu\text{m}$ $1\text{-}\sigma$ precision, moving the arm as required, and stitching all of the data together, using button measurements to compensate for systematics introduced by moving the CMM around the table. This is on the order of the smallest of the tolerances in the error budget, and fitting directly to error budget terms was expected to pull the most critical terms out of the noise.

After the project began, the plan was altered to have the final measurement done at Allied with a DEA Delta Slant gantry CMM large enough to measure the entire petal with $\sim 0.5\mu\text{m}$ $1\text{-}\sigma$ precision, much smaller than any tolerance in the error budget, and with no need to shift the CMM.

- (2) *Improved propagation tools.* The Bessel-function propagator originally slated for use with the TDEM required a number of artificial constraints, due to the limitations of the approach. In particular, it evaluated a number of integrals in the radial variable r , and the petal edge had to be specified at the same r on both sides of the petal. This is a difficult requirement, particularly when the CMM must be physically moved to measure opposite sides, and so fitting to a set of analytically-defined error budget terms and extracting the width from those was expected to make this calculation possible. Switching to a line-integral propagator eliminated the requirements on even spacing, however, and as the noise properties were much improved by the use of the Allied CMM, the need to fit error-budget terms in order to produce an electric field at the telescope aperture was eliminated.

After applying this technique to the full edge data, we propagated the field through a telescope—assumed to have an unobscured aperture—to the image plane, and calculated a figure of merit: we found the mean contrast in an annulus centered at the inner working angle (90mas) and with a width corresponding to the full-width-at-half-maximum of the point spread function of the telescope. This was done in 10nm increments across 250-500nm passband of the occulter, and the worst of these numbers was taken as a conservative estimate of the worst-case contrast. For the occulter as built, **the worst case contrast was 2.15×10^{-10}** , occurring at 380nm. Figure 20 shows the image-plane intensity at 380nm, and Figure 21 shows the mean contrast in the annulus as a function of wavelength in the passband.

It is important to remember the conservatism of this milestone. As can be seen from Figure 21, wavelengths below 380 nm perform significantly better than the worst case and above that remain below the 2×10^{-10} value. In addition, as seen in Figure 20(b), the contrast value is taken right at the smallest inner working angle. Because of the rapid fall-off of the PSF, the contrast quickly improves for only small increases in angle. This again points to the conservatism of our error budget. For instance, one could design a slightly oversized occulter with a smaller inner working angle than required to produce relaxed requirements for the operational inner working angle. As we pointed out earlier, our approach in this TDEM has been to design, build and test the smallest occulter possible for the given mission requirements to verify feasibility.

To verify the milestone we need to find the 95% confidence level of contrast. In other words, it is possible that the contrast calculated by the mean of the measurements combined errors in such a way that our performance appears deceptively good, while in truth the shape of our petal does not meet the milestone. To find the 95% confidence value we developed a model of the measurement error based on the Allied calibration data for the CMM. Systematic errors in CMM runout were fit and removed, and random errors in the measurement were then modeled based on

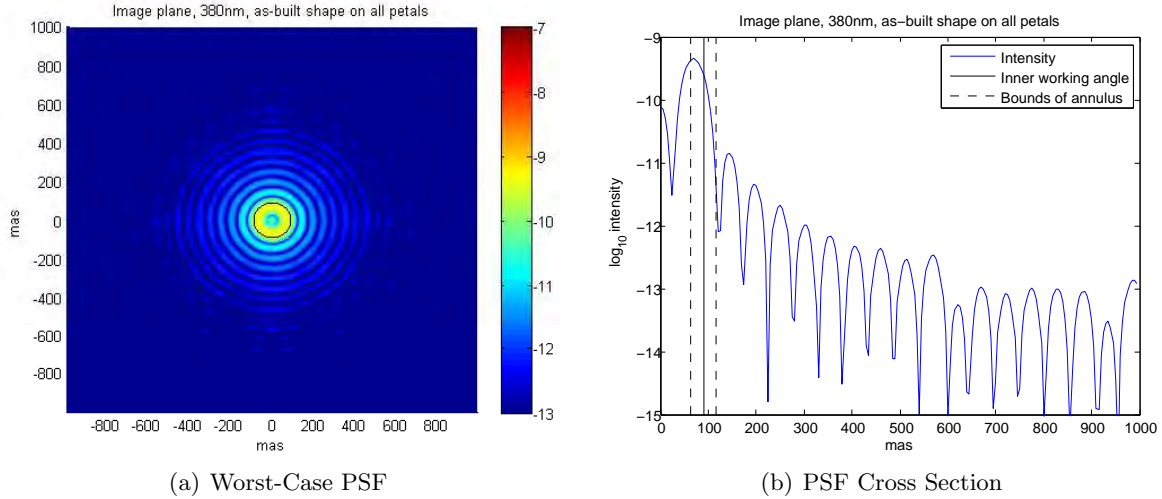


FIGURE 20. (Left) The image-plane intensity profile at 380nm for an occulter with 30 identical petals, plotted with a log stretch. The inner working angle is shown with a solid circle. While the occulter is assumed to be spinning, this represents an instantaneous snapshot of the intensity. (Right) A cross section of the point-spread function showing the designed inner working angle and the boundaries of the annulus used for contrast calculation.

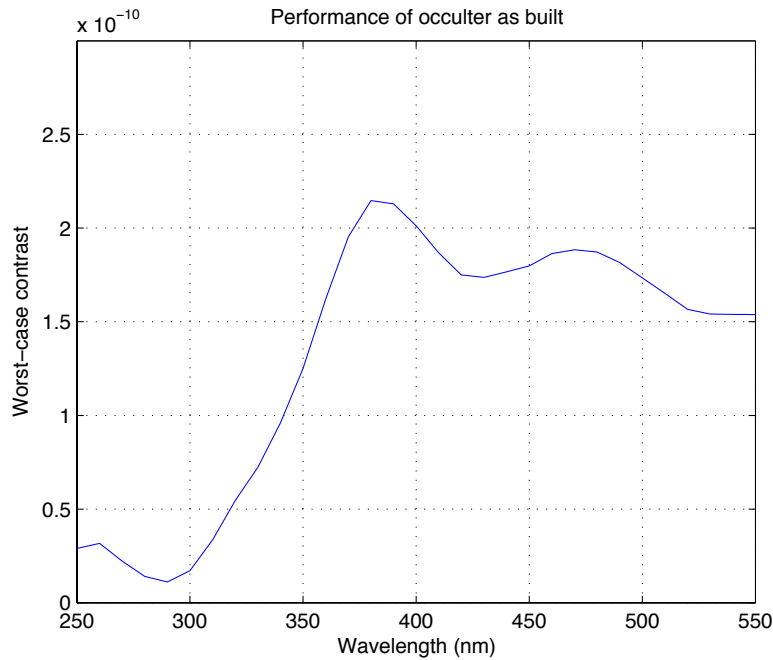


FIGURE 21. A plot of mean contrast in an annulus about the IWA for an occulter with 30 petals identical to the one built, plotted as a function of wavelength. The worst case is at 380nm, when the mean is 2.15×10^{-10} .

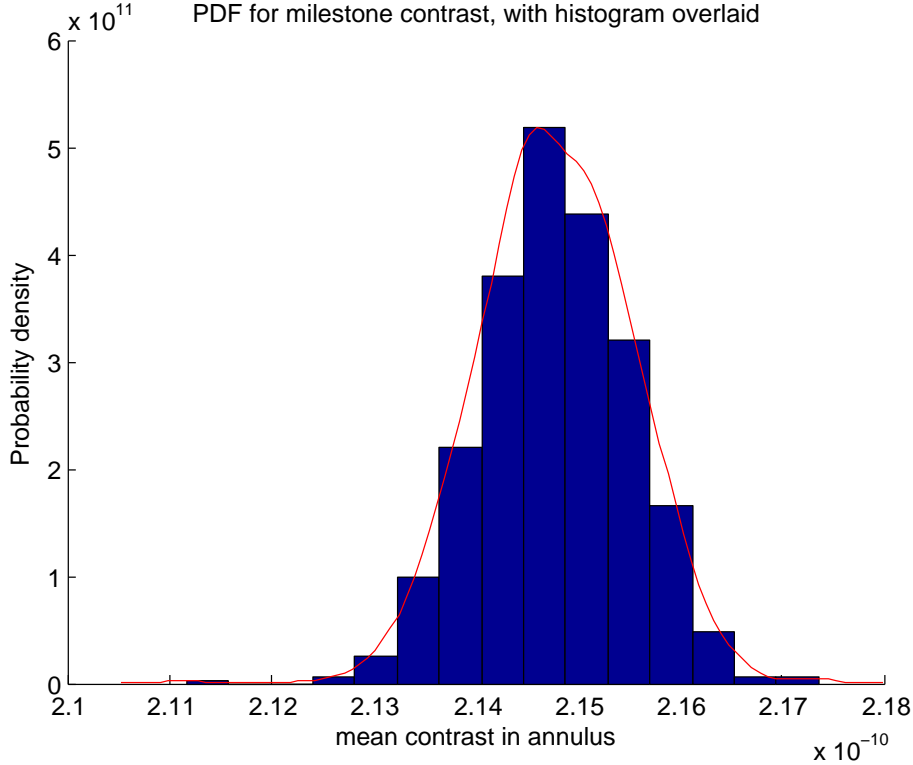


FIGURE 22. Probability density function (PDF) for the true contrast produced by an occulter made from identical copies of the existing petal. The overlaid histogram shows the data produced by the Monte-Carlo simulation, representing 700 separate sets of measurement errors. The y-axis normalized the probability density such that the integral over the PDF is 1.

the residuals. We used this measurement model as the input to a Monte Carlo simulation, where measurement errors consistent with these models were repeatedly applied to the mean of the Allied data. We then evaluated the worst-case mean contrast in an annulus for each of these perturbed data sets. This served to build up a probabilistic model of contrast values consistent with both the petal and the measurement tools; the resulting probability distribution function (PDF) is shown in Figure 22 along with the histogram of Monte-Carlo data. The probability that the contrast $c > 3 \times 10^{-10}$ —that is, the milestone was not actually met—was numerically indistinguishable from zero. In addition, we find that there is a 95% probability that the true mean-contrast-in-an-annulus is less than 2.16×10^{-10} , bettering our milestone by 30%. Full details of the analysis to find the measurement error distribution are given in Appendix B.

7.2. Performance Estimation for Non-Identical Petals. The results in the previous section assumed each petal on the occulter was identical to the as-built. This is highly conservative and results in an over-estimate of contrast as identical errors rectify around the circumference. A more realistic simulation would populate the occulter with 30 petals containing random errors consistent with the as-built and corresponding error budget. This would also be consistent with the error budget we discussed in Section 4.2. We do this by decomposing the measured data from the segment edges into various error budget terms (for example, amplitude at 2 cycles/meter) and randomizing the amplitude for each segment on each petal around the occulter. This is possible because we can estimate the distribution of manufacturing errors based on the 10 measured optical edge segments.

	Perfect structure	As-built structure
Perfect segments	3.1×10^{-12}	1.2×10^{-11}
As-built segments	2.5×10^{-10}	2.1×10^{-10}

TABLE 4. Worst-case contrast in an annulus about the IWA for four cases: with and without the distortion of the petal structure, and with and without the differences between the ideal edge segments and the shape as built.

Doing so, however, requires that we assume that each fitted error-budget term on each segment is drawn from the same underlying distribution. In the absence of any other information, this is the only reasonable assumption; with only a single petal manufactured, treating each term on each segment as independent precludes any form of extrapolation. This assumption is not entirely unjustified, as each segment is applied along the petal edge using an identical procedure: the segment is placed by adjusting the buttons on both ends of the segment independently, aiming to match the offset specified in the GUI. The ends are then clamped, and the segment is bent in the center to bring the center segment button to the correct offset as well. For comparison, the structure bend, discussed subsequently in Sec. 7.2.1, has only a single data point associated with its fitted parameters, and we will not attempt to extrapolate from that point.

7.2.1. *Decomposition into structure and edge terms.* After the contrast for the designed petal was determined, some question remained as to why the final contrast estimate was so close to the milestone given the very low contrast (from 1.2×10^{-11} to 6×10^{-11}) computed from the preliminary estimates based on the segment shapes as measured by Hexagon (see Section 5.3.2). Two possible sources are the errors in the segment placement and/or counterbend of the segments, or from the distortion of the petal structure on which the segments are bonded.

Both of these can be seen to be present: the measured buttons on the petal structure do not align perfectly between the first (Aug 2011) and second (Feb 2012) measurements at Allied Mechanical, and the measured points along the edges of the petal segments do not align perfectly with the designed petal shape. Figure 23 shows the offsets of the measured edge position from the ideal at each point. Visible is a significant uniform bend of the structure (to the right on the lower half and to the left on the upper half).

We remove the systematic error in the edge profile due to the distortion of the petal structure by fitting the x - and y - discrepancies in button positions between the first and second Allied runs with a pair of polynomials for each edge, one for each coordinate. Subtracting these systematic bends produces the plot shown in Figure 24, with the residuals given in Figure 25. Note that the different segments can be seen clearly, and that most of the large-scale deformations were from the distortions in the frame. However, we note also that the petal-structure deformation is primarily width-preserving, a mode which is known [6] to produce little effect on the contrast when all petals have the same shape. To estimate the relative effect on contrast due to the structure bend, we recomputed the contrast for an occulter with 30 identical petals for four cases: with and without the effects of structure bend, and with and without the effects of segment errors. The results are shown in Table 4. All of these use the February Allied data for the measurements. It appears that some of the structure bend served to compensate for the layout of the segments, though the milestone would have been met even without the distortion present.

7.2.2. *Contrasts from fitted terms.* In order to fit terms in the error budget we extracted the components of each vector in Figure 24 (with the structure bend removed) normal to the local slope of the petal edge at that point; these are given in Figure 26. As a model, we chose to fit a piston and tilt on each segment (to cover translation and rotation) and a number of sinusoids along the edge to cover the bend, counterbend, and residual manufacturing and placement errors. Testing

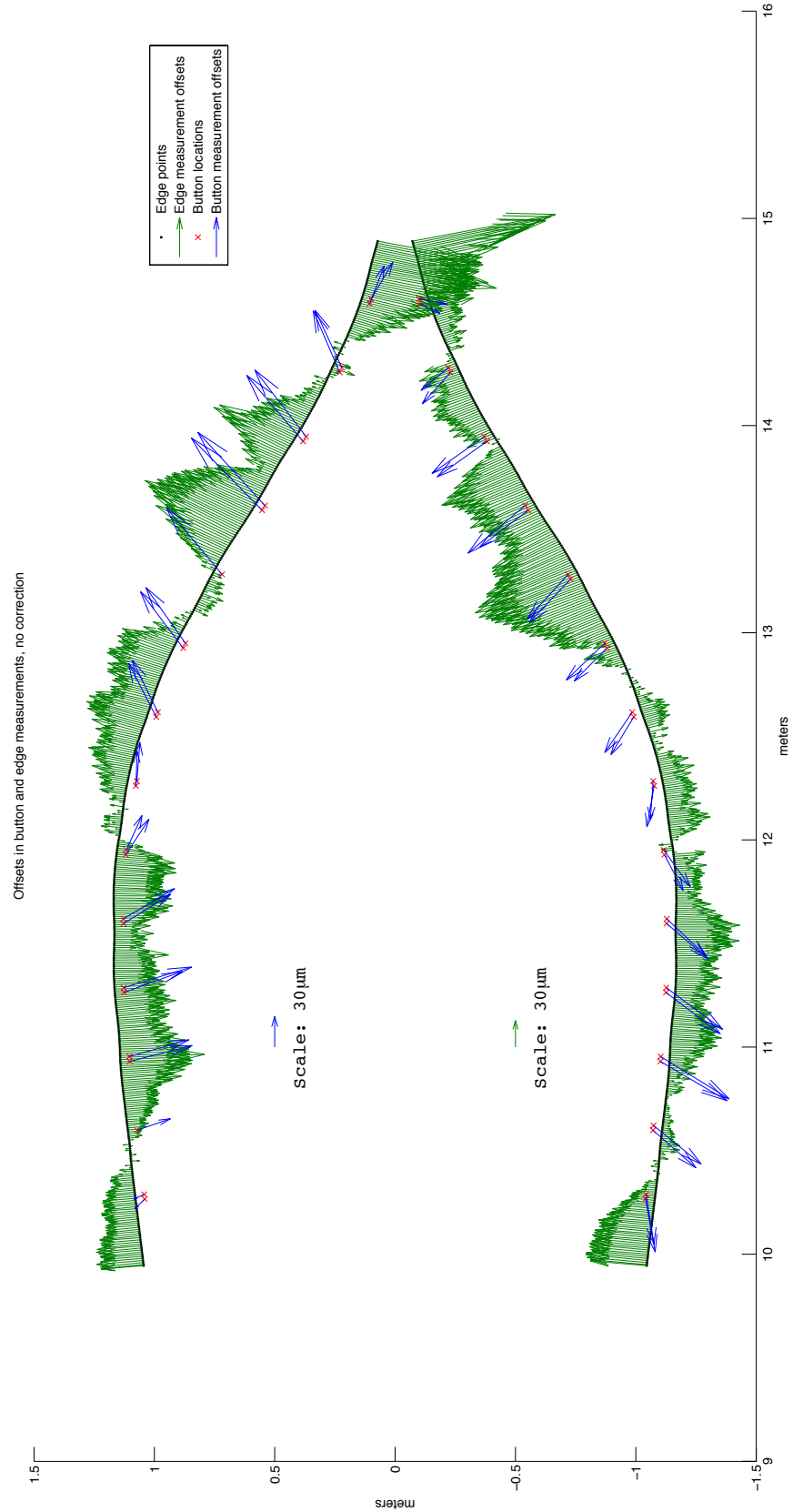


FIGURE 23. Measurement deltas with both petal structure deformation and segment errors. Displacements of the buttons (shown as red \times s) between the first and second measurements at Allied are shown in blue; the difference between the ideal petal shape and the shape measured at Allied are shown in green.

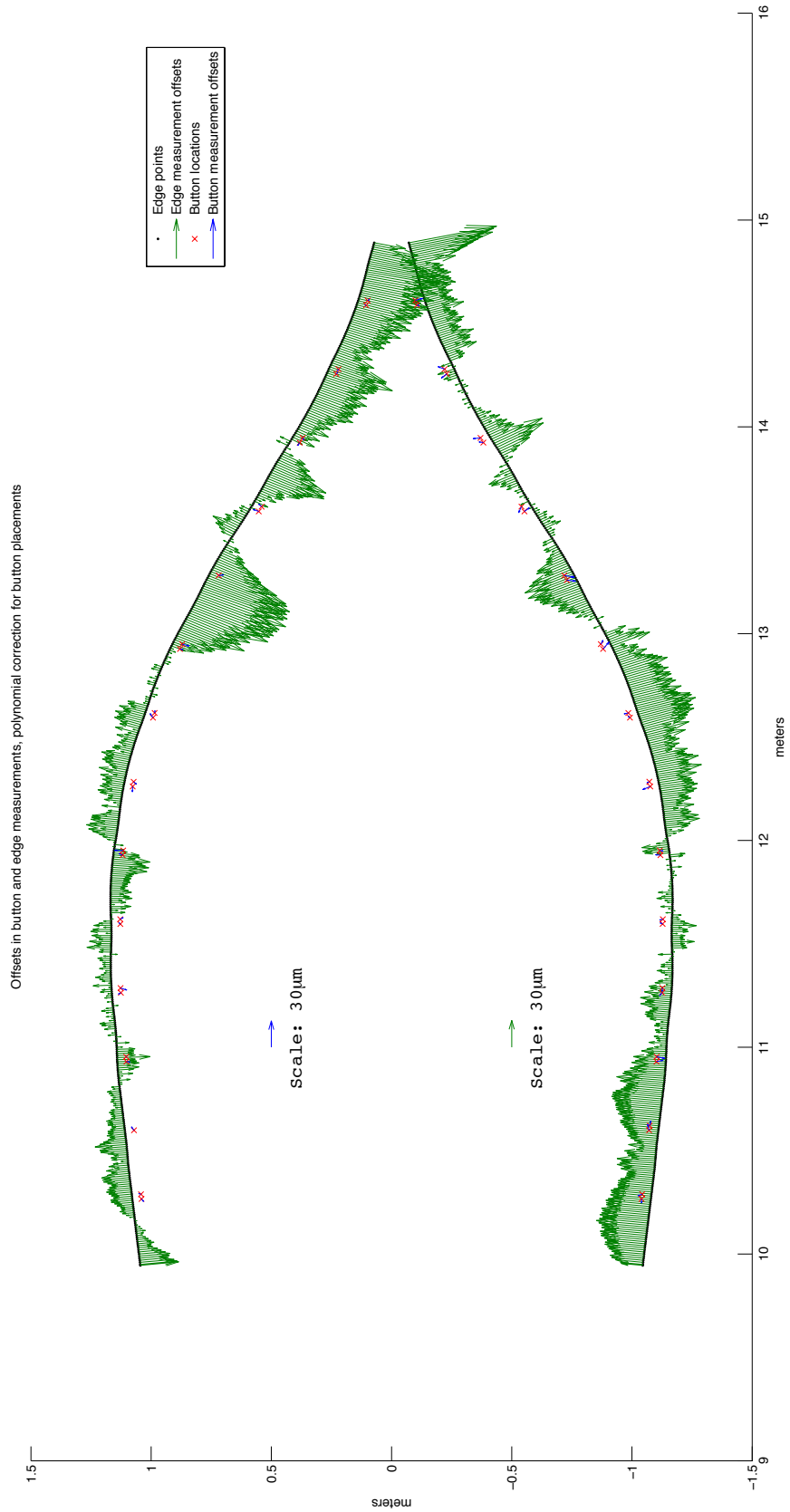


FIGURE 24. Measurement deltas with segment errors only, the structure deformation having been fit out. Displacements of the buttons (shown as red \times s) between the first and second measurements at Allied are shown in blue; the difference between the ideal petal shape and the shape measured at Allied are shown in green.

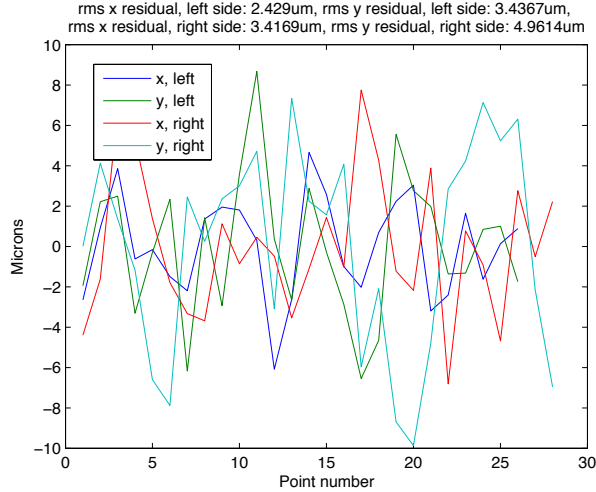


FIGURE 25. Residuals from the polynomial fit to the structure buttons, running from the base of the petal to the tip.

Perturbation	rms Amplitude
Segment δy	15.2 μm
Segment Tilt	25.3 μrad
1 cycle/segment	11 μm
2 cycles/segment	14 μm
3 cycles/segment	5 μm
4 cycles/segment	5 μm
5 cycles/segment	3 μm
6 cycles/segment	3 μm

TABLE 5. The rms of the fitted amplitude of the most significant perturbation terms on the as-built segments, averaged over the 10 segments. Cyclic terms assume both a sine and cosine wave are present.

showed that including frequencies up to 10-12 cycles/meter along the segments would be sufficient to capture the edge shapes as measured. The discrepancy between the measured and ideal shape for each segment was fit with these terms. The fits are given in Figure 27, and the fitting residuals are given in Figure 28. It is worth noting here that comparisons with the Hexagon measurements of the edge show that the large bends on segments 1, 3, 6 and 8 were successfully compensated for but that additional low frequency error was introduced during installation, as discussed in the previous section.

Table 5 shows the rms averaged amplitudes of the most significant fitted perturbation terms, averaged over all 10 segment fits. A comparison with Table 2 shows that all are below the allocation for a 10^{-10} star shade with the exception of segment tilt that is only slightly above. This implies that an occulter made up of random petals with errors consistent with the measured as-built petal segments (with the structural bend removed) should meet the contrast allocation for manufacturing errors of 1.5×10^{-11} (the structural bend and placement errors are allocated a separate contrast). In fact, a Monte-Carlo analysis using the mean and standard deviations of the perturbations from the 10 as-built segments assuming Gaussian distributions (as explained in Section 4.2) results in a mean contrast due to manufacturing error of 1×10^{-11} .

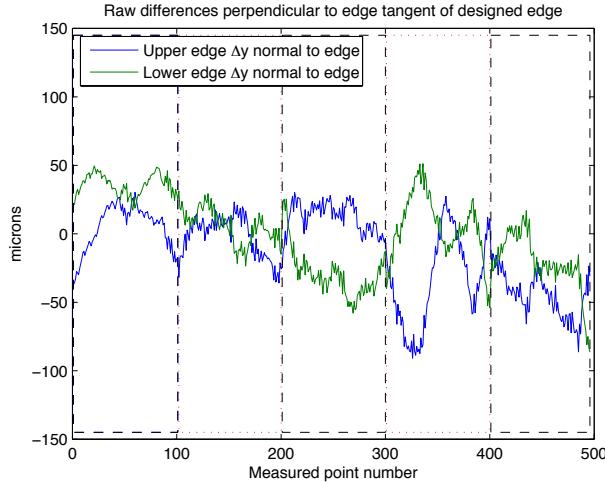


FIGURE 26. The normal components of the vectors in Figure 24; red and black boxes separate the points on each of the five segments.

Because there is no *a priori* reason to assume that the distributions of the various segment perturbations are Gaussian, a more accurate analysis uses the measured segments to estimate the probability distribution of each term. A Monte-Carlo analysis then creates new edge segments for the 30 petals by drawing errors from each of these distributions. We thus returned to kernel density estimation to create the probability density function for each fitted term. We used a rule-of-thumb estimator for the kernel bandwidth [11]:

$$b = 1.06 \min \left(\hat{\sigma}, \frac{\hat{R}}{1.34} \right) n^{-1/5} \quad (1)$$

where n is the number of data points, $\hat{\sigma}$ is the sample standard deviation, and \hat{R} is the sample interquartile range. We choose this estimator as it is both fast and makes few assumptions about the underlying distribution. (We only have 10 unique data points, so there is little justification for using a more complex technique.)

As the amplitude of each sinusoid cannot be negative, we modified the density estimation procedure for these cases by using a reflection approach[12]. The data set was doubled to include each point x and the corresponding $-x$; the density estimation is done on this modified data set to give a PDF f^* . We then drew from the PDF f defined as:

$$f(x) = 2f^*(x), \text{ for } x \geq 0 \quad (2)$$

$$= 0, \text{ otherwise} \quad (3)$$

The phases of the sinusoids were consistent with a uniform distribution between 0 and 2π and were drawn from such. Rather than draw the slope and intercept coefficients directly, we transformed these variables and created a distribution of offsets of each end of a segment from 0. Given that each end of each segment was placed independently, we feel this was a more reasonable approach than coupling them through the coefficients of the linear fit directly. Points drawn from this distribution were transformed back into linear terms to produce the additional modeled segments.

Figure 29 shows a sample simulation of the resulting image-plane intensity at 380nm. Figure 30 shows the resulting distribution of contrasts under the same metric as the manufactured petal (worst-case wavelength, mean of an annulus around the inner working angle) using 50 occulters simulated under the conditions specified above. Two cases were run: one assuming a perfect underlying structure (which should result in a contrast corresponding only to the manufacturing

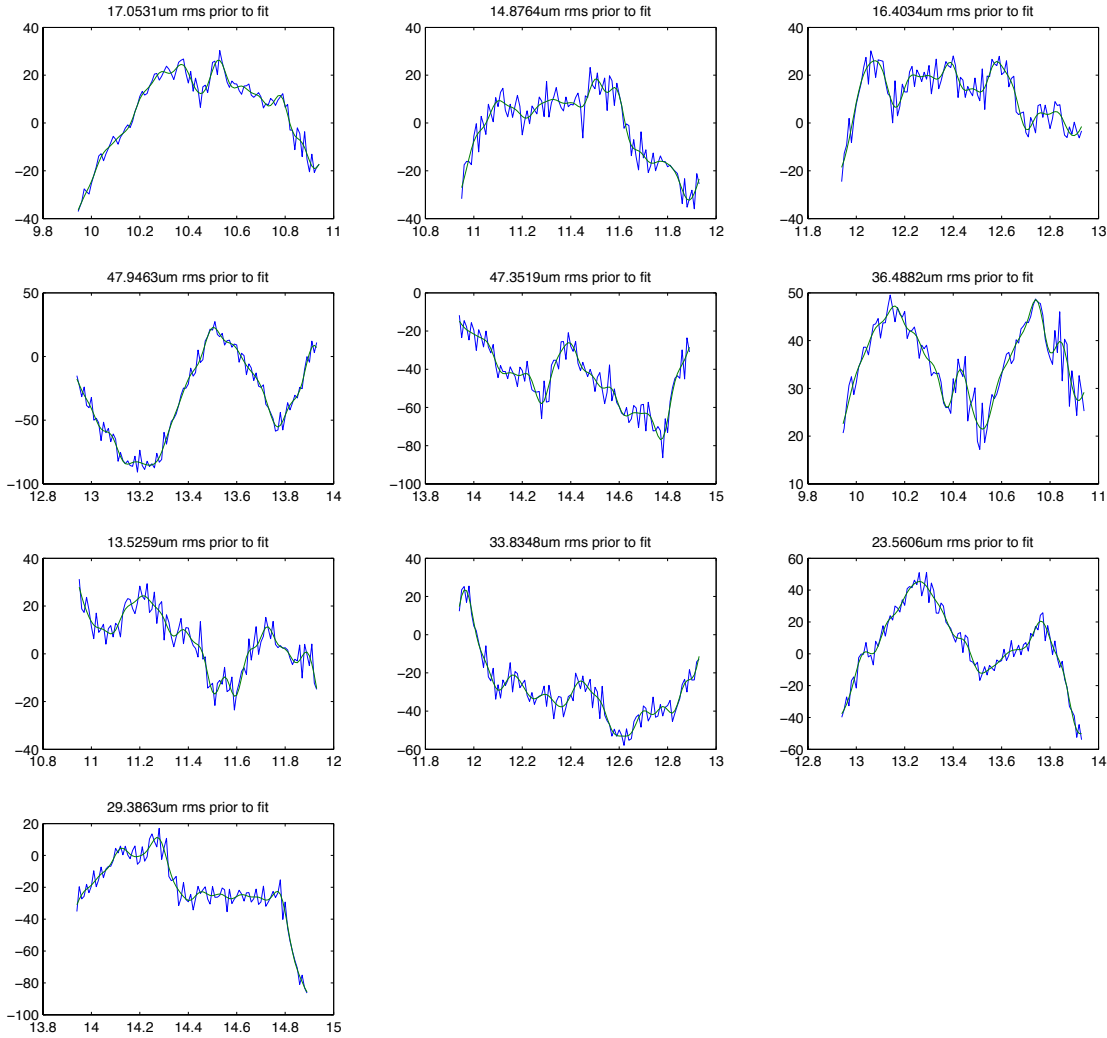


FIGURE 27. Fits to the 10 segments given in Figure 26, using a piston, tilt, and 12 sinusoids from 1 to 12 cycles/meter.

errors described in Section 4.2) and one with each petal having the identical structural bend to that seen in the as-built petal. We again note the strong assumptions under which these extrapolations were derived, but should those assumptions hold, the modeling suggests that occulter performance will be improved by a factor of more than 10 from the milestone case. Here the expected value of the contrast (assuming a perfect structure) is 2.12×10^{-11} and the 95% confidence value is below 4×10^{-11} . This is slightly larger than the allocation for the flight occulter, but only by a small amount, and gives considerable confidence in our ability to manufacture an occulter to the needed specification.

8. MATERIAL COUPON TESTING

We have also conducted materials tests of representative samples of the M-55J carbon composite used for the TDEM petal. The principal goal of these tests was to assess whether the level of microcracking of the material as the petals are stowed or deployed (or even as they are handled during assembly) is likely to cause a problem with meeting the tight dimensional tolerances required

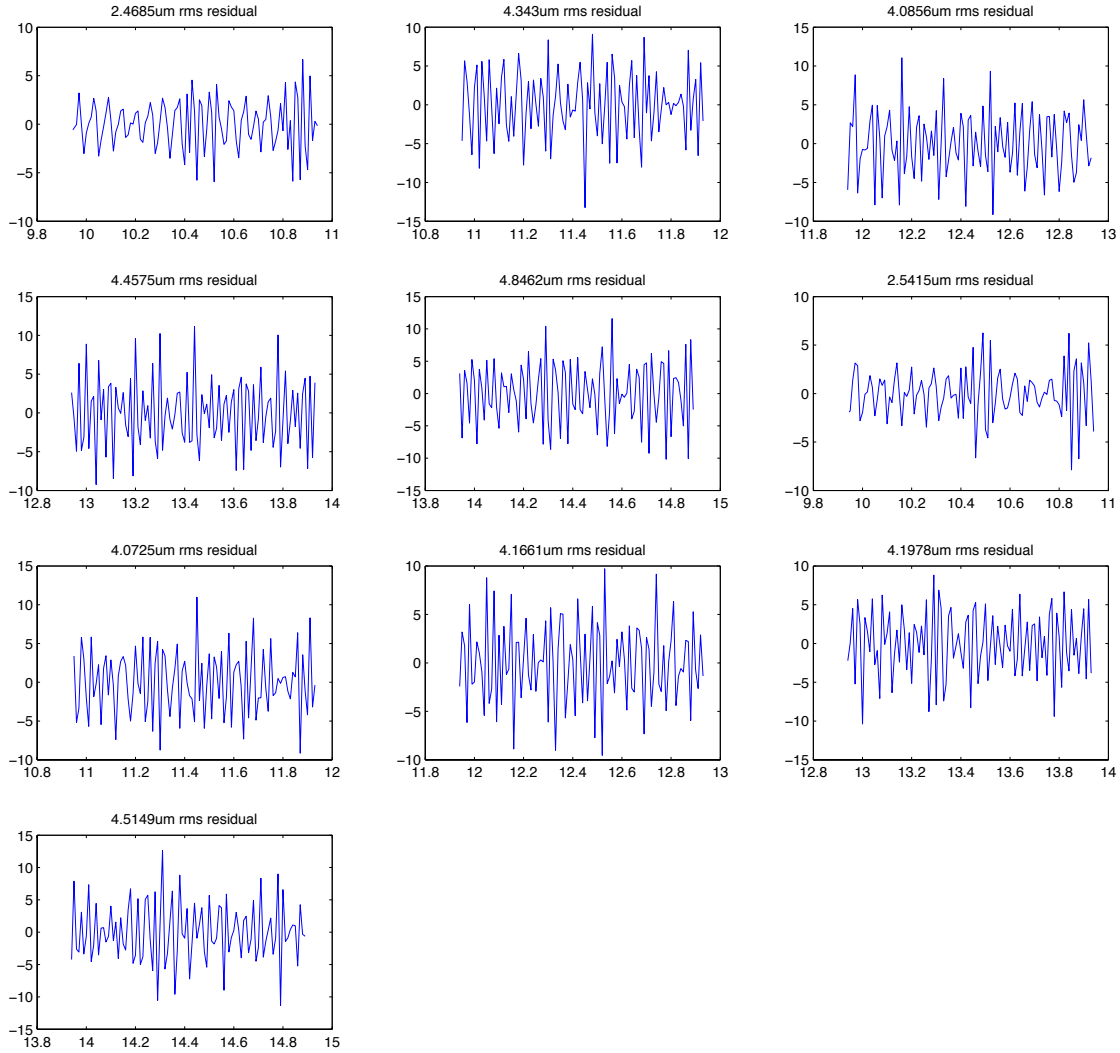


FIGURE 28. Residuals from the fits to the 10 segments given in Figure 27.

for starlight suppression. Cracking can cause unexpected deformation, and the cracks can act as reservoirs for gases. It may also lead to roughening of the optical edge whose sharpness minimizes undesirable scattering of light. We used mechanical tests, microscopy, acoustic tomography and small-angle x-ray scattering (SAXS) to characterize the microcracking. These tests found no large cracks (> 100 microns) at bending strains up to 0.5%, the strain at which audible popping occurred. Recall that the petal is designed so that no parts are strained by more than 0.5% during stowing and analysis of the current design shows a maximum strain of only 0.2%. The stress-strain curves did not display any anomalies until a precipitous drop in stress at a strain of $\sim 1.2\%$ due to the formation of a transverse crack. Analysis of SAXS data is on-going which will quantify microcrack distributions at the sub-micron level. We also note that the targeted material for flight, M-46J, has a much higher strain capability. Appendix C describes in detail the material testing process and results.

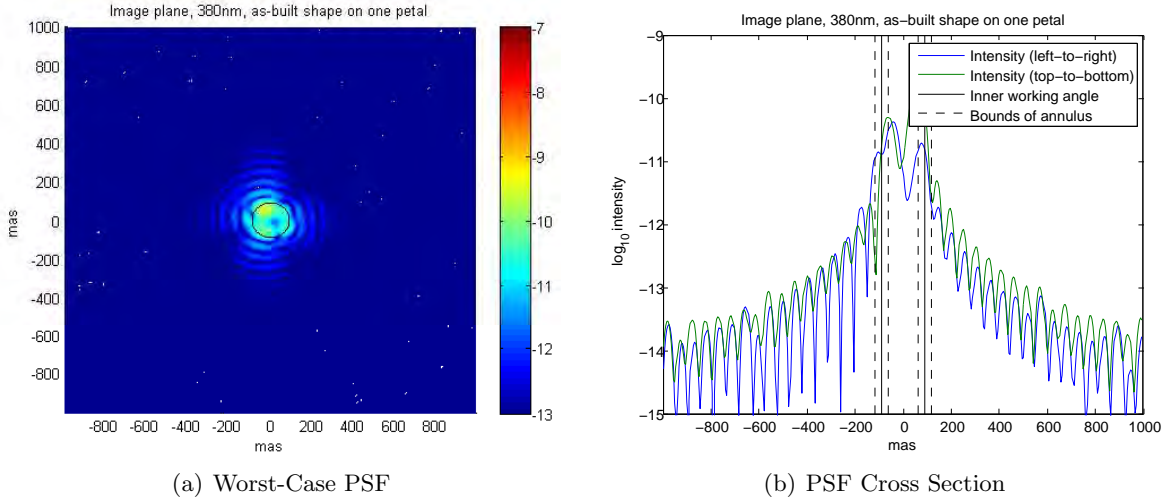


FIGURE 29. (Left) The image-plane intensity profile at 380nm for an occulter with 30 random petals, plotted with a log stretch. The inner working angle is shown with a solid circle. While the occulter is assumed to be spinning, this represents an instantaneous snapshot of the intensity. (Right) A cross section of the point-spread function showing the designed inner working angle and the boundaries of the annulus used for contrast calculation.

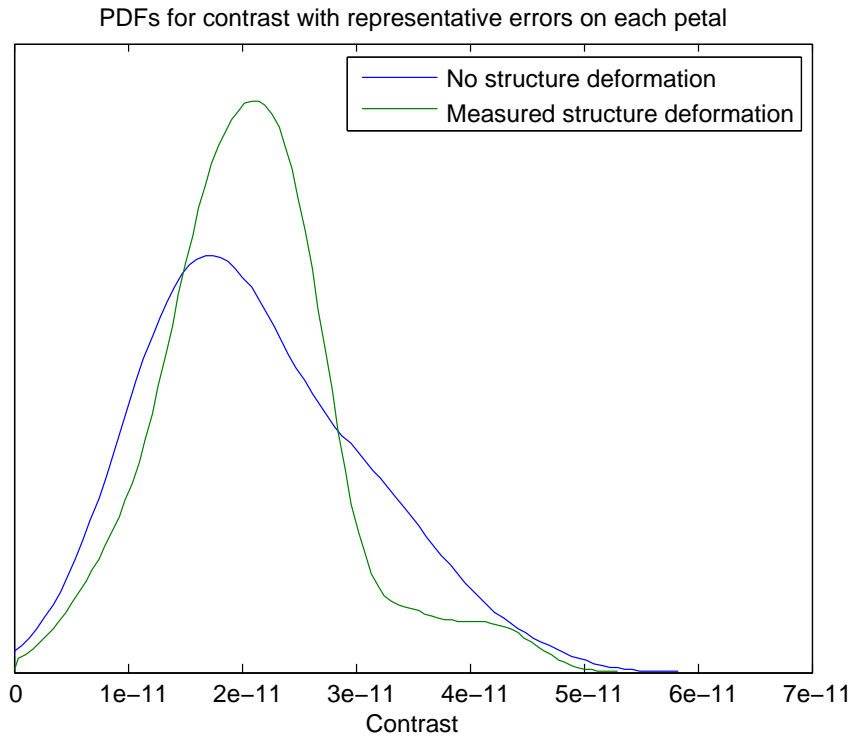


FIGURE 30. Distribution of worst-case mean contrast, assuming random errors consistent with the placed segments are applied to each segment on each petal independently. The two cases shown are with and without the overall petal deformation seen in the petal as built.

9. CONCLUSIONS, LESSONS LEARNED AND FUTURE WORK

As shown in this report, we exceeded our milestone goal by 30% in contrast at the worst case wavelength and closest inner working angle for the conservative case of a single set of global errors on all petals equal to that on our measured as-built petal. For the more realistic case of an occulter with random errors on each petal consistent with those seen on the as-built petal we achieved a calculated mean contrast at the inner working angle more than an order of magnitude better than the milestone (more than a factor of 5 better at the 95% confidence level). We have shown that it is possible to build an occulter petal to the stringent shape requirements for a terrestrial planet finding mission.⁶

As noted in various places in both the whitepaper and this report, we do not claim to have developed an optimal design and manufacturing process for the occulter petal. For instance, more exploration of cutting techniques and metrology methods is certainly warranted. Our goal was only to demonstrate that a design exists, that it can be built to the stringent requirements needed for an occulter mission, and that existing metrology techniques are sufficient to demonstrate performance. In that we succeeded. More importantly, we learned a great deal about the design and manufacture of petals that can be applied to future work on starshade missions. In the remainder of this section we list the most important of them and the key directions needed in future work on petal manufacturing. In a second TDEM just getting underway we begin work on the next challenging design and manufacturing issue for occulters—deployment of a petal and truss combination to the needed millimeter level accuracy.

9.1. Lessons Learned.

- (1) Edge installation: The process of controlling the edge segment position at two end-points and one mid-point proved effective at those control points but the edge shape was significantly deformed in between these points. This effect is illustrated in Figure 27 with a clear “W” pattern to the edge position errors. One solution would be install a test jig to the edge segments that makes the edges behave as rigid bodies.
- (2) Metrology targets: The conically shaped metrology targets proved effective for the tool used during installation where a ball probe is seated into the cone by hand, but is less effective using an automated CMM machine that does not have the requisite dexterity. A workable solution was derived as part of this activity but an improved target design should be considered.
- (3) Structural deformation: The petal structure shape changed significantly between the initial and final metrology measurements, as shown in Figure 23. Note that all of the errors outboard of a certain point are shifted in one direction and all of the errors inboard of that point are shifted in the opposite direction. This is a shearing effect and likely results from the limited effectiveness of the longerons to provide in-plane shear strength as result of the long aspect ratio of the petal. This remains to be confirmed by analysis and experimentation but if this was the cause a relatively simple design to fix it is to add some crossing members to the structure. Note that this shape deformation is largely width preserving, as the battens are relatively stiff, and does not have a large impact on contrast performance, but the problem should be addressed none-the-less.

9.2. Future Work.

- (1) Demonstrating manufacturing shape tolerances after deployment. This was a goal of this TDEM, but was deferred due to cost constraints. This should be performed after resolving lesson learned item 3 above.

⁶Experiments are being undertaken in the laboratory at Princeton to verify the validity of the numerical optical modeling used to compute the contrast from the shape.

- (2) Demonstrating edge scatter performance and developing a manufacturing process for creating a beveled edge with the desired radius of curvature. This also was a goal of this TDEM, but was deferred due to cost constraints.
- (3) Related to item 2 above is the need to develop a harder material that would be compatible with a grinding process. This involves optimizing the resin chemistry.
- (4) Develop petal tip section. This is not considered a difficult problem due to the reasonably large minimum width of 2 mm and the greatly relaxed tolerances at the outermost part of the petal, but was not addressed in this TDEM due to cost constraints.
- (5) Development of an automated, in-situ metrology process to support the fabrication of a large number of flight petals. This can be addressed in Phase A.

10. ACKNOWLEDGEMENT

This work was completed under a grant from the National Aeronautics and Space Administration (NASA), grant no. NNX10AF83G.

APPENDIX A. SUCCESS CRITERIA FROM WHITEPAPER

While establishing an error budget and formulating requirements on petal shape is essential, and an integral part of our TDEM activities, the ultimate objective is to achieve sufficient starlight suppression. Our approach is therefore not to provide a comprehensive comparison of the measurements to a derived error budget, but rather to set as our success criteria a confirmation of (a slightly relaxed) mean image plane contrast of 3×10^{-10} at the geometric inner working angle were a full starshade to be built to the measured accuracy of our petal with all other terms in the error budget set to zero. We will establish success using the analytical process described and the following combination of metrology and modeling:

- (1) Perform measurements of the shape of each side of the petal relative to a fiducial origin in Cartesian coordinates along each edge as described in Sections 3.3 and 3.5.2 with measurement error quantified as in Section 3.3.
- (2) Transfer the measurements to a common coordinate system and convert to polar coordinates as described in Section 3.4.
- (3) Perform a fit to confirm that the measurements fall within the range of the requirements in Table 3 from the error budget as finalized by the time of the final measurements as described in Section 3.4.
- (4) Steps 1—3 must be satisfied on three separate occasions with at least 24 hrs between the end of one set of measurements and the beginning of the next set of measurements.
- (5) Take a set of measurements and generate a set of measured errors either by fitting or by subtracting an interpolated petal shape from the nominal shape.
- (6) Using our optical modeling tool, propagate an incident plane wave past the simulated occulter to the image plane of the corresponding telescope. Repeat the monochromatic analysis for a selection of three or more wavelengths in the designed-for passbands, including the maximum and minimum design wavelengths.
- (7) Calculate the mean contrast over an annulus of width equal to the full-width half-max of the telescope point spread function at the inner working angle at each wavelength.
- (8) Repeat steps 5, 6, and 7 N times to produce N values of contrast from N measurement sets, with N determined by a statistical power test. Perform hypothesis testing as described in Section 3.5.2 to determine whether a starshade composed of copies of the manufactured petal would provide $\leq 3 \times 10^{-10}$ contrast at the inner working angle across the passband.

APPENDIX B. ALLIED MEASUREMENT CALIBRATION AND STATISTICAL MODELING

B.1. Calibration data. One potential challenge when providing a value for expected occulter performance is the possibility of erroneously claiming that the measurement data was consistent with the milestone, when this result is in fact only an artifact of measurement error. This is known as a *Type I error* and it cannot and should not be ruled out *a priori*. Rather, we wish to show that the probability of this happening is less than some desired threshold.

In statistical terms, the null hypothesis is that the worst-case mean contrast, c , is greater than 3.00×10^{-10} . The milestone is to reject this null hypothesis with 95% confidence—that is, with a probability of a Type I error, α , of 5% or less. To do this, we can use independent knowledge of the errors in the metrology used to measure the petal to produce a probability distribution function (PDF) of performance consistent with both the data measured and the noise properties of the measurement device. From this function, we can estimate (1) the probability of a Type I error for the initial null hypothesis, and (2) the contrast level consistent with a Type I error of 5%.

Calibration data for the Allied coordinate measuring machine (CMM) was taken in August 2010 by a third party with a Renishaw interferometric calibration system. Differences between commanded and actual position were measured at 200mm intervals up to 5m in the x -direction, and in 100mm intervals up to 2.5m in the y -direction, three times apiece in each case. (Differences in the z -direction were measured as well.) These measurements are shown in Figure 31.

The systematic trend was fit by a set of splines through the mean of the three measurements in both x and y individually, to allow the systematic error to be estimated for distances other than those explicitly calibrated. These spline curves are also shown in the plots in Figure 31; the curves for the x -axis and y -axis systematic errors had peak-to-valley amplitudes of $4.6\mu\text{m}$ and $3.8\mu\text{m}$, respectively. In subsequent processing of the final Allied data, these curves were subtracted from every Allied measurement to compensate for the variable CMM bias with distance.

The three repetitions of the calibration had a small spread to them, as well. The differences between the measured value and the spline curve at each point were used to estimate a probability density function for the random errors in measurements. We note that the random errors in the Allied metrology system are significantly smaller than the expected errors from the FARO metrology arm, which we had expected to use at the outset of this work—the RMS residual after subtraction of the systematic bias was $0.73\mu\text{m}$ in the x -direction, and $0.62\mu\text{m}$ in the y -direction. These residuals serve as the basis for the subsequent development of the PDF.

B.2. Shape error distributions consistent with measurements. To simulate petal shapes with errors consistent with our measurements, we need more than the mean error; we must choose a distribution from which to draw errors in measurement. After subtraction of the mean calibrations, 78 residuals remain in the calibration data along each of the x - and y -axes: three sets of 26, corresponding to 26 x and y positions in the CMM. Our challenge is to take these residuals Δx and Δy and build a new distribution from which we can repeatedly draw new, consistent measurement errors for each of the points along the optical edge of the petal. This is then used in a Monte-Carlo simulation to determine the distribution of contrast.

As a first guess, we might assume that all 78 are drawn from a single identical distribution, which would greatly simplify the creation of consistent data. This hypothesis cannot be rejected with an α of 5%. However, we can also look at the correlations of each the three sets of Δx to their associated measurement location x , defined as cross-covariance of the two vectors scaled by the square root of the product of their auto-covariances:

$$[C]_i = \frac{\text{cov}(\Delta x_i, x)}{\sqrt{\text{cov}(\Delta x, \Delta x)\text{cov}(x, x)}} \quad (4)$$

Here i goes from 1 to 3 and cov is the covariance operator (i.e., equivalent entry of the covariance matrix). Calculating this gives us off-diagonal elements of magnitude 0.6209, 0.0521, and 0.6494 for

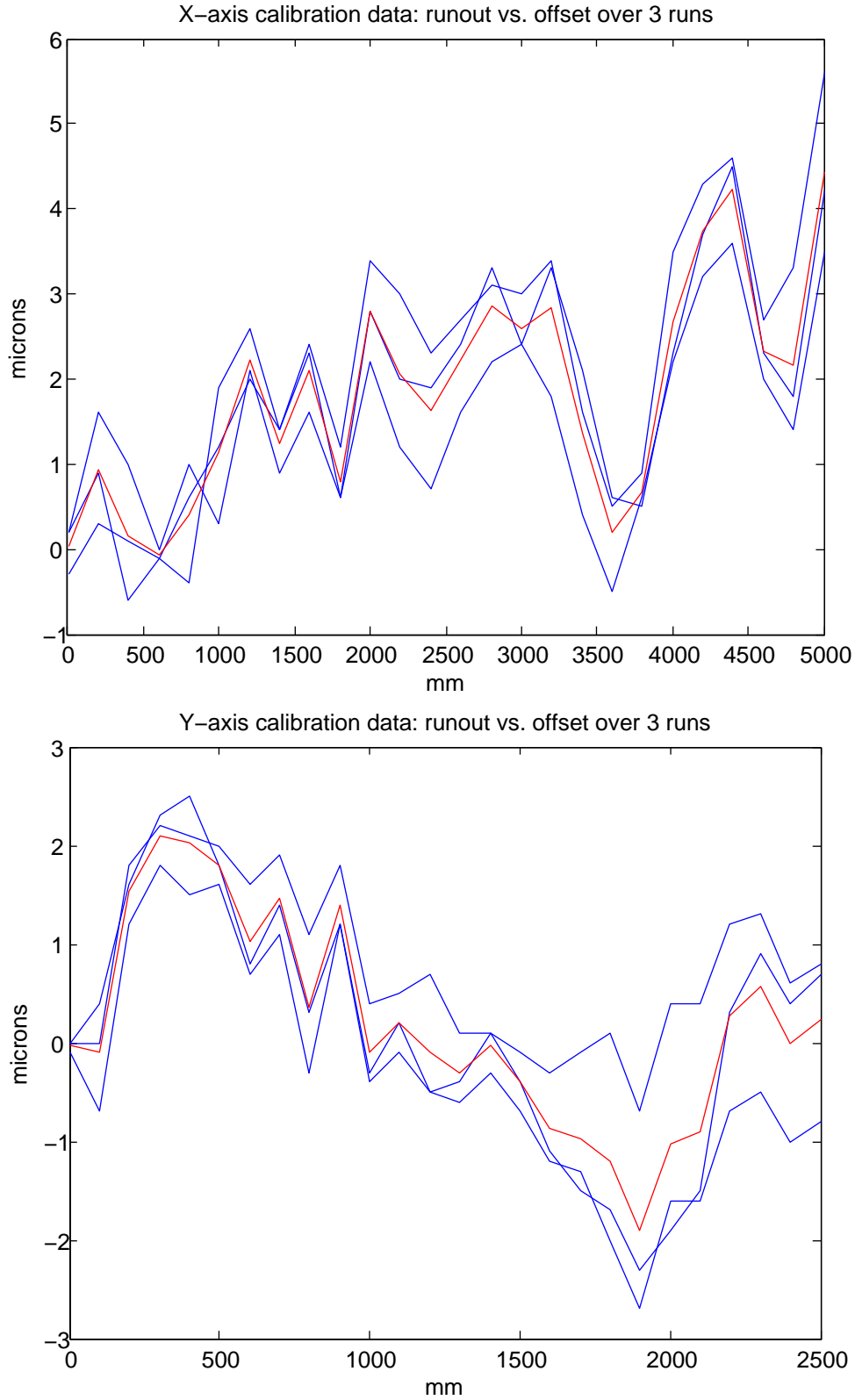


FIGURE 31. Errors in the measurement at different positions across the Allied CMM, along the X (top) and Y (bottom) axes. Three sets of data were collected and are shown in blue. A spline fit to the data, used for interpolation, is given in red.

the three x dimension data sets, respectively. The equivalent p -values⁷ for the no-correlation null hypothesis in the first and third case are 0.0007 and 0.0003, so we can reject this null hypothesis at the 5% level and assume that there is a correlation between the Δx values and the measurement location, which would be lost if we sampled these from a single distribution.

Given this, we can try a different assumption: each set of three measurements represents a distribution of errors at that measurement location. Given the data, this hypothesis cannot be rejected at the 5% significance level, and by the Lilliefors test, each set is consistent with a normal distribution.[13]. Thus, to sample the errors along the entire length of the petal, we take standard deviation σ of each set of three Δx and Δy and fit a cubic spline to these as a function of position x or y . To sample the measurement error at a given point, we then simply draw a random value from the normal distribution defined by $N(\mu(x), \sigma(x))$ or $N(\mu(y), \sigma(y))$, using the splines fit in Sec. B.1 as the position-varying mean μ . This is illustrated in Figure 32.

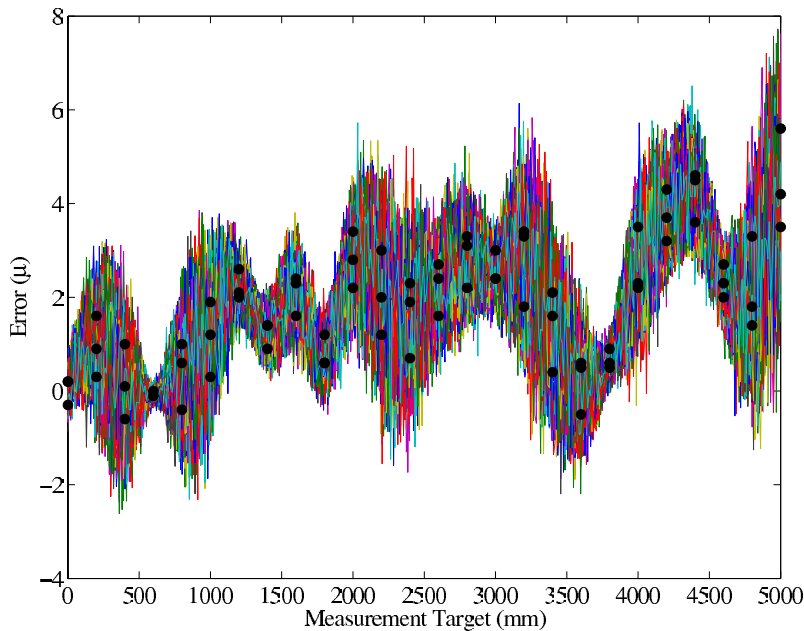


FIGURE 32. Original measurements (black points) and 200 consistent, sampled shapes (colored lines).

My rewrite: CMM random measurement errors were repeatedly drawn from these distributions and added to the mean of the five occulter shape measurements at the measured points in the line integral. This procedure was repeated 700 times with the mean contrast in a $1\lambda/D$ -width annulus centered on the IWA as the figure-of-merit.

To assess the probability that an occulter constructed of petals identical to the one measured generates a maximum contrast of 3×10^{-10} at all wavelengths, we can calculate the probability that the contrast produced by a sample petal shape is greater than the target contrast:

$$P [c > 3 \times 10^{-10}] = \int_{3 \times 10^{-10}}^{\infty} f_{\bar{c}}(c) dc, \quad (5)$$

where \bar{c} is the random variable representing the contrast produced by an occulter whose petals are identical to one that is consistent with the measured petal, with density function $f_{\bar{c}}$. To find $f_{\bar{c}}$,

⁷A p -value is the probability that a particular value would be observed, assuming our chosen null hypothesis is true. If the p -value is less than α , then we reject our null hypothesis.

we use kernel density estimation (KDE) on our sample of calculated contrasts to estimate the continuous probability distribution from the discrete and finite set of Monte Carlo data points. Using the same methodology as before, we can show that the contrast results for separate wavelengths represent non-identical distributions, so we can operate on the results of individual wavelengths.

Following [14], we employ a maximum likelihood estimator to find the best values for the location (\mathbf{m}), bandwidth (\mathbf{b}) and weight (\mathbf{w}) values, defining the kernel density estimate as

$$\hat{f}_{\bar{c}}(c, \mathbf{m}, \mathbf{w}, \mathbf{b}) = \frac{\sum_{i=1}^n w_i K_{b_i}(c - m_i)}{\sum_{i=1}^n w_i}, \quad (6)$$

where K_{b_i} is the standard normal density kernel with bandwidth b_i , and the sum is taken over all Monte Carlo points. Applying this method on the sampled contrast values from the wavelength producing the largest mean and standard deviation of contrasts yields the results in Figure 22; the PDFs for the top five contrasts are in Figure 33.

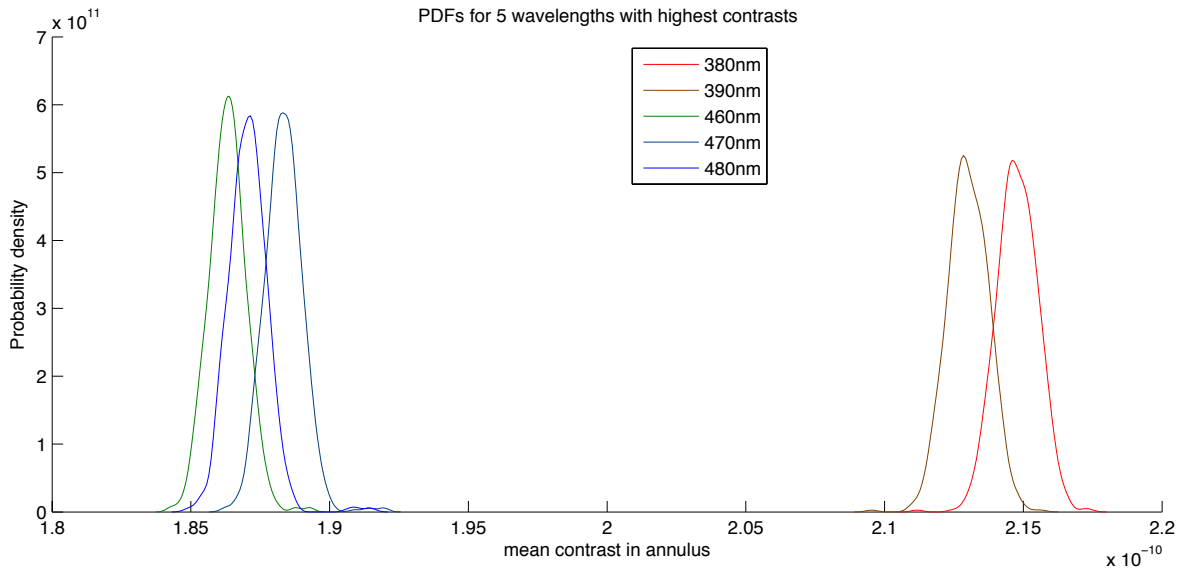


FIGURE 33. Probability density function of contrasts for the five wavelengths with largest mean contrast values.

For all wavelengths within the passband of the occulter, the probability that $c > 3 \times 10^{-10}$ is smaller than the minimum accuracy of the numerical data type (IEEE 754 floating point) used, and so numerically indistinguishable from zero. Given this, **we can confidently state that the predicted mean contrast in the image plane from a uniform field propagated past an occulter with petals of the measured shape in an annulus of width equal to the full-width half-max of the telescope point spread function at the smallest inner working angle is 3×10^{-10} or better.**

We can also examine the tails of these PDFs to determine at what point we reach a 5% probability of a Type I error. At the worst case wavelength (380nm), there is a 95% probability that the true contrast is less than 2.16×10^{-10} ; for all other wavelengths, the probability that the true contrast is less than 2.16×10^{-10} is greater than 95%.

APPENDIX C. MATERIAL SELECTION AND TESTING

C.1. Overview. As materials are put under a load, they may undergo deformation that is irreversible; e.g. a bend that does not completely straighten when the load is removed. For composite materials that irreversible deformation may be due to cracking or creep. Creep results from the flow of defects in the material over a long period of time in response to the stresses in the material. Cracking may occur due to tension, such as at the outer radius of a bent longeron (mode 1 fracture). It may also occur due to shear (mode 2 fracture). In composites, fracture often occurs at the interface of the fiber and the matrix. The fibers are quite strong compared to the interface, and mode 1 or mode 2 fracture can occur at the interface. In compression, fiber composites suffer from a buckling failure in which the fibers buckle and the fiber-matrix interface fails. A large crack may run entirely across a structural element, causing failure of that element. Even without complete failure, cracks at the microscopic level can cause deformation of the material and they can be reservoirs for absorbed gases. Since the efficacy of the occulter requires tight dimensional control, it is a concern to have even small levels of irreversible deformation or deformation that relaxes slowly as the material out-gases.

Bending of fiber composites is often accompanied with a popping sound due to micro-fracture events. Small cracks form at the fiber-matrix interface during deformation producing this sound. The tough matrix may prevent these cracks from running across the structural member and causing complete failure, but the micro-cracks accumulate under continued fracture. Experiments in the literature have characterized carbon-carbon composite micro-cracking using the acoustic emission method [Bussiba 2008a, 2008b]. The material they studied is similar to, but not identical to, the kind of composite best suited to the starshade petals. They placed a sample in a rig for flexural and bending tests and recorded acoustic emission events as the sample was deformed. They found that fracture began at about 0.1% strain (1000 μ strain). Siron et al. [Siron 1999] have also used acoustic emission to study fracture processes in carbon composites. For comparison, the design specs for the starshade petals are that no component is subjected to more than a 0.5% strain and the battens are subjected to \leq 0.05% strain in stowing, deployment or operation.

We have conducted experiments to characterize micro-cracking in starshade petal composite materials subjected to strains representative of petal stowage and deployment. In particular, we have conducted 4-point bending tests and used optical microscopy, acoustic tomography, small angle x-ray scattering (SAXS) to determine the extent and character of micro-cracking in the composite samples. The tomography has been done both prior to, and following, deformation in a 4-point bending rig. The SAXS measurements have been performed on a series of samples deformed to different strains from as-received to beyond the threshold for audible cracking. The goal is to determine the initial crack/void density (or put an upper bound on it) and the threshold strain for further micro-cracking.

C.2. Sample Specification. We have tested 15 straight cut test samples 12.7 mm wide x 50.4 mm long x 0.48 mm thick fabricated by Patz Materials & Technology specifically for this TDEM project. The material consists of layers of M55J high-modulus carbon fibers embedded in resin rotating by 60 deg from layer to layer. Both surfaces have the fibers oriented transverse longitudinal axis (which we indicate as 0 deg). These samples are representative of the kind of composite materials that will be used for the optical edge of the starshade, with an opportunity for further optimization of the materials going forward in order to obtain slight improvements for the CTE and mechanical properties. The carbon composite is also similar in some respects to what would be used for the structural elements (battens and longerons), but the layup tested here is different than that of the pultruded structural rods.

C.3. Bending Tests. Bending tests have been performed in order to subject the samples to a specified level of strain in bending for subsequent characterization of the extent of microcracking.

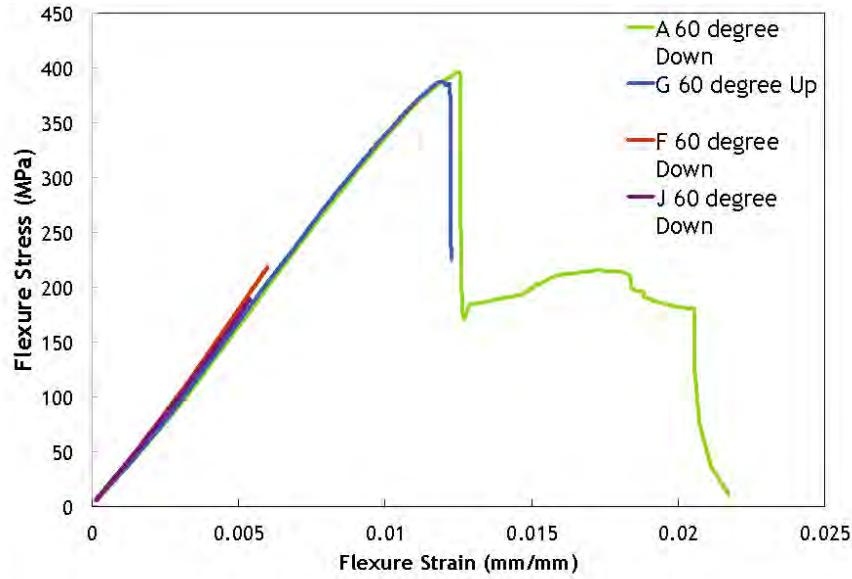


FIGURE 34. Stress-strain curves measured in the 4-point bend tests. The stress-strain curves from 4 samples are overlaid for comparison. The samples are nominally identical, apart from sample G being arranged in the bend test differently, with the surface with the 60 degree texture up rather than down. The notation 60 degree up or down refers to the orientation texture pattern on the specimen surface with respect to the transverse direction. The fibers are perpendicular to the long direction of the specimen on both of the outer surfaces. The samples were strained to different levels and then unloaded for further analysis to determine the microcracking at those strain levels. Sample A was strained to fail completely due to multi-layer fracture.

The bending tests also provide a stress-strain curve for the materials. These 4-point bend tests were conducted on an Instron 5900 (an electromechanical screw driven loading machine) with a 2 kN load cell, guided by the ASTM standard D6272 [ASTM 2010]. The support span was 30 mm and the load span 10 mm. The bending tests were run at a displacement rate of 3.48 mm/min. The displacement of the sample was measured using a laser extensometer model LE-05 which has a range of 10 mm full scale. A more detailed description of the method used for bending tests is given in Ref. [ASTM 2010].

The stress-strain curves obtained in the 4-point bend tests are shown in Figure 34. The initial part of each curve at small strains represents elastic deformation. For sufficiently large strains, microcracking occurs. At a strain of 0.005 audible popping sounds were detected that were attributed to microcracking. At a strain of 0.012–0.013 a large transverse crack formed causing the precipitous drop in stress apparent on curves A and G in Figure 34. Sample A was taken to complete failure at a strain of ~ 0.022 . This failure strain agrees with the value reported by Baral et al. for another M55J composite to within the error bars [Baral 2008]. The stress-strain curves for the 7 SAXS samples are shown in Figure 35.

C.4. Optical Microscopy. Optical micrographs of the carbon fiber composite have been taken prior to, and after, bend testing. Most of the samples showed no evidence of damage due to the bending tests. Samples G and B exhibited a transverse surface crack that spanned the width of the sample but did not cross through the thickness. These samples showed a drop in stress at a strain of ~ 0.012 , as shown in Figure 34 and Figure 35, respectively. An optical micrograph of the fracture is shown in Figure 36. The image also shows the rough surface of the sample in the left

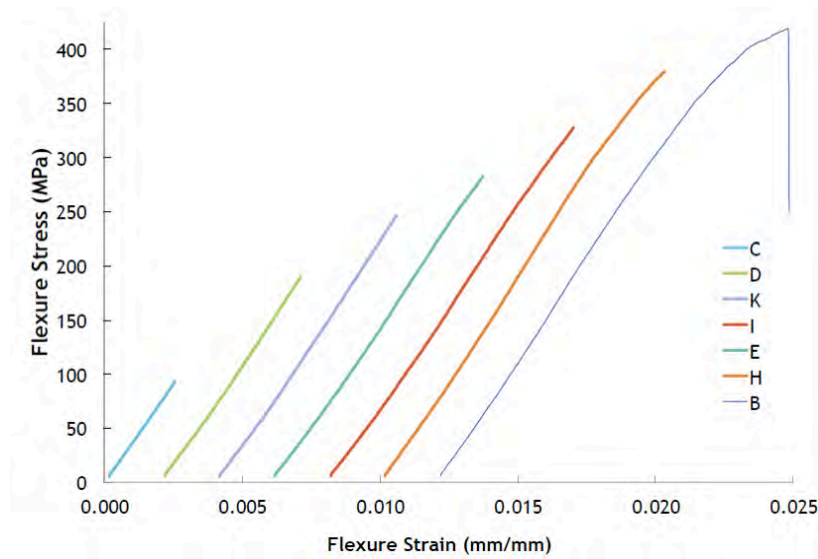


FIGURE 35. Stress-strain curves measured in the 4-point bend tests: the 7 samples for SAXS measurements (offset horizontally to separate the curves). All samples were loaded with the same orientation. The samples were strained to different levels and then unloaded for further analysis to determine the microcracking at those strain levels.

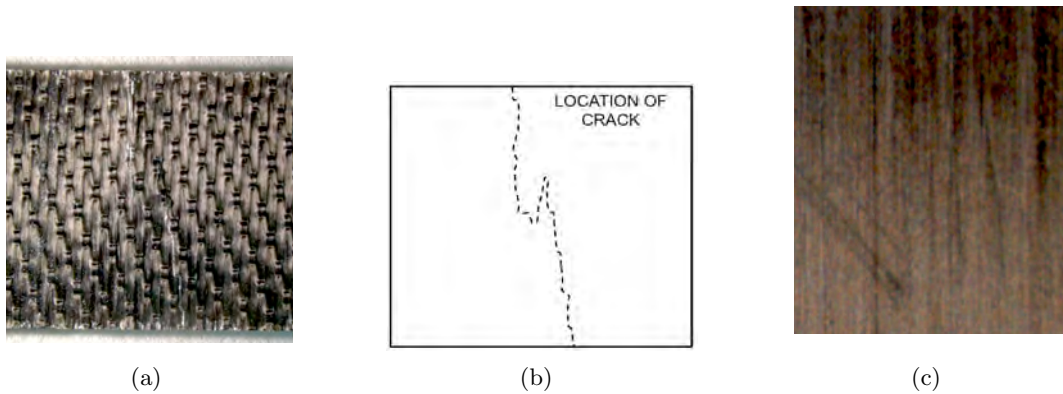


FIGURE 36. (left panel) Optical micrograph of a sample of the carbon fiber composite sample G, subjected to a bending strain of 0.012 causing fracture of the surface fiber layer. The stress-strain curve for this sample is shown in Figure 34. The fracture did not propagate into the lower layers of the composite. The entire 12.7 mm width of the sample is visible top to bottom. (center panel) A schematic illustration of the morphology of the crack. (right panel) The opposite surface of the samples is smooth.

panel. This roughness was present in the as-received sample and is the result of the fabrication process. The opposite surface is smooth, as shown in the right panel.

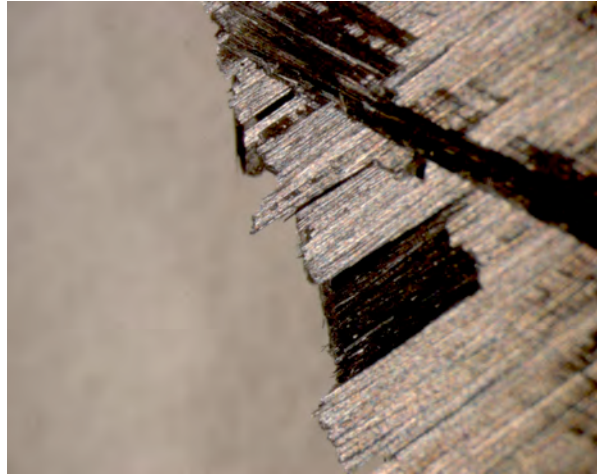


FIGURE 37. Optical micrographs of the carbon fiber composite materials. Fractured edge of a sample taken to complete failure (the green curve of Figure 34). A rough fracture is visible, exposing different layers of the composite.

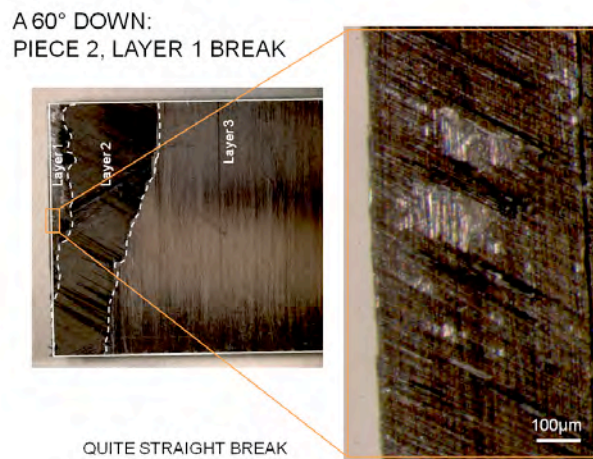


FIGURE 38. A close-up view of the fracture surface at the rough side of sample A. Layers 1, 2 and 3 indicate the rough face, interior and smooth face, respectively.

Sample A was subjected to a strain of ~ 0.022 and failed completely. The rough edge of the resulting fracture is shown in Figure 37. The different layers of the composite fractured at different locations and with different morphologies, as shown in Figure 38, 39 and 40.

C.5. Acoustic Tomography. Acoustic tomography tests were performed in order to characterize relatively large cracks by imaging (cracks > 100 microns) and by the total level of acoustic attenuation (cracks > 1 micron). The acoustic tomography was performed on a sample subjected to a strain of 0.005, the level of strain at which audible popping but no visible crack occurred in the 4-point bend test. Acoustic tomography is a kind of non-destructive testing. In these tests, acoustic waves are run through a sample in order to detect and map inhomogeneities within the sample. The samples are immersed in a fluid that provides acoustic coupling to the sample. We have used water. A high frequency transducer produces acoustic waves that propagate through the fluid, into the sample where there is some loss due to absorption or scatter, back into the fluid and

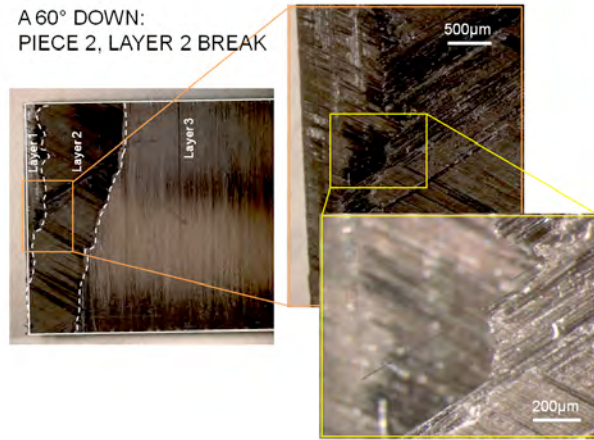


FIGURE 39. A close-up view of the fracture surface at the interior of sample A. The different layers of the composite are visible.

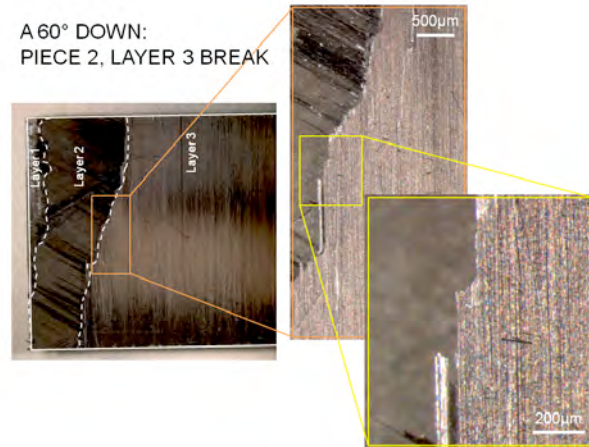


FIGURE 40. A close-up view of the fracture surface at the smooth surface of sample A. The transverse orientation of the outer fibers is visible.

are then detected by another transducer in the fluid. Any variations in the acoustic impedance of the material induce scattering and/or absorption of the waves, and the attenuation of the acoustic signal can be used to construct a map of the heterogeneities in the material including cracks and voids. If the material has many small cracks that are too small to image, it is possible to infer the extent of microcracking from the level of acoustic attenuation. Due to the wavelength of the acoustic waves, the technique can only image cracks and other inhomogeneities down to about 100 microns in size. The technique is sensitive to the overall population of cracks larger than about 1 micron through the total attenuation of the signal. It provides a valuable test of the integrity of the as-received materials and whether large cracks form as a result of the bending tests. A review of the acoustic tomography technique is given in Ref. [Birks 1991].

The parts were acoustically scanned using an industrial pulse-echo immersion scanner (Panametrics). The scan recorded the point to point transmission amplitude loss through the thickness of the composite coupon. The color differences indicate attenuation of the acoustic signal through the material thickness due to material differences. The 15MHz transducer was chosen after several

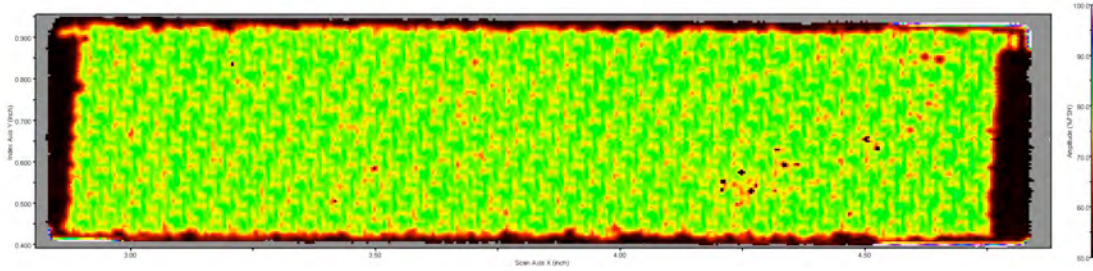


FIGURE 41. Acoustic tomography map of the fiber composite materials. The coloring corresponds to the amplitude of the acoustic signal, as indicated in the color bar to the right. No microcracking was observed at strains up through the threshold for audible cracking at a strain of 0.005. The pattern observed in these images is due to acoustic scattering from surface roughness. The dark areas at the edges of the specimen are where it was supported in the tank.

attempts to reveal the layup pattern. This will not image individual fibers, (too small) just larger features on the order of $100\mu\text{m}$.

Results of the acoustic tomography tests are shown in Figure 41. No microcracking was observed at strains up through the threshold for audible cracking at a strain of 0.005. The pattern observed in these images is due to acoustic scattering from surface roughness. These findings exclude the formation of large cracks > 100 microns in size.

C.6. Small-Angle X-Ray Scattering (SAXS). SAXS measurements use x-ray scattering to detect inhomogeneities in a sample. A bright x-ray source generates monochromatic x-rays that scatter off variations of the electron density in a sample, including the drop of the electron density in a crack or void. The scattered x-rays are recorded on a 2-dimensional flat X-ray detector situated behind the sample with the plane of the detector perpendicular to the direction of the incident x-ray beam. The scattering pattern is analyzed to determine information on the structure of the sample. The SAXS technique is sensitive to cracks from a few nanometers up to a ~ 100 nm. Another technique, Ultra-Small-Angle X-ray Scattering (USAXS), is sensitive to larger cracks up to a micron. In either technique, the beam can be positioned at different points in the sample in order to determine spatial variation in the crack size distribution. A monograph is available that describes the SAXS technique in detail [Glatter and Kratky 1982].

We have used the Advanced Light Source (ALS), Beamline 7.3.3, at the Lawrence Berkeley National Laboratory to obtain SAXS data for the starshade carbon composite material. Figure 42 shows the scattering pattern. The 6-fold symmetric scattering pattern is due to the $(60^\circ, 0^\circ, -60^\circ)$ layup of the composite. The individual fibers are 7 microns in diameter, so they are too large to affect the SAXS signal. The six-fold symmetry is a result of anisotropy of microcracks and smaller features along the interface of the fibers and the resin matrix.

In order to relate the SAXS data of Figure 42 to a microcrack size distribution a quantitative analysis is needed. Standard SAXS analysis packages assume that the defects causing the scattering are isotropic and homogeneous throughout the region expose to the x-ray beam. The six-fold scattering pattern shown in Figure 9 is clearly not isotropic, so a generalized analysis is needed. The approach is to consider the SAXS intensity at a specified angle chosen to be sensitive to the dimension of the microcracks running along the fiber-matrix interface.

Several lineouts through the scattering data are shown in Figure 43. These lineouts correspond to two positions on sample B, one at the center of the loading span and one at 4 mm from the center. The scattering intensity was summed as a function of the scattering wavevector q at the

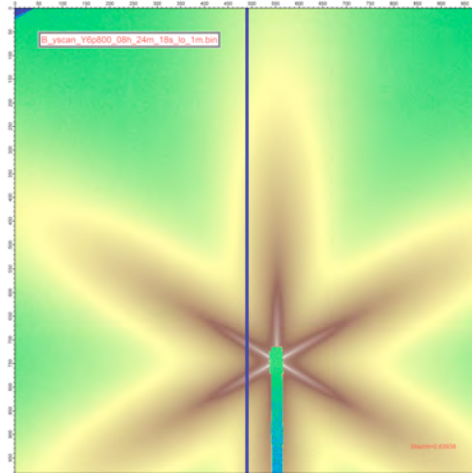


FIGURE 42. Small-angle x-ray scattering (SAXS) plot for the carbon composite sample B, the sample subjected to the largest strain of the 7 SAXS samples. The 6-fold symmetric scattering pattern is due to the $(60^\circ, 0^\circ, -60^\circ)$ layup of the composite. Sections through the scattering pattern were used to determine the microcrack distribution.

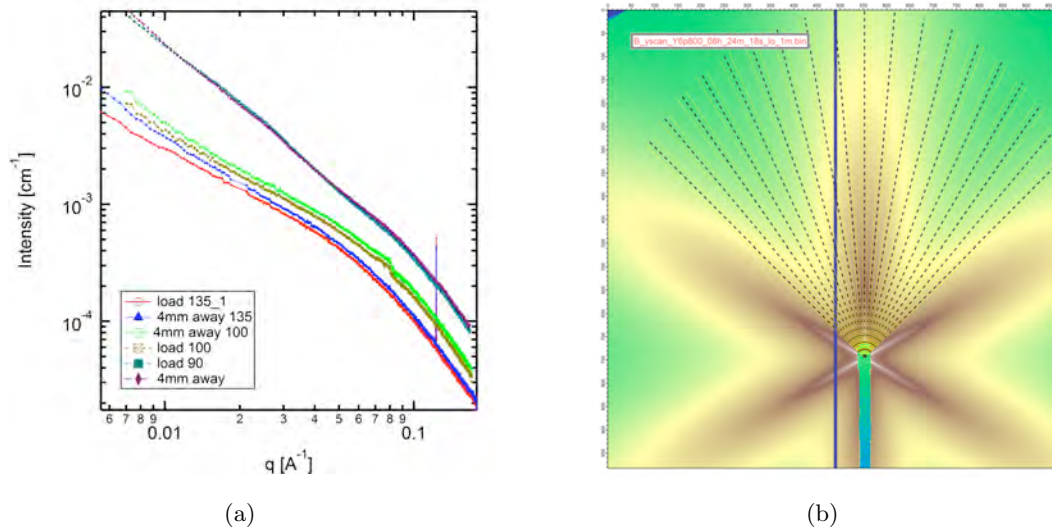


FIGURE 43. Lineout from the SAXS scattering intensity (Figure 42).

angle indicated $\pm 1^\circ$. The two highest intensity curves correspond to the scattering data through the center of the lobe at the two positions on the sample. With this reduction of the data, the analysis can proceed using standard techniques. In general, the goal is to relate the scattering intensity to the properties of the sample, in this case the cracks. For example, in the Guinier regime the scattering intensity can be related to the radius of gyration of the scatterers according to [Putnam 2007]

$$I(q) = I(0) \exp(-q^2 R_G^2/3) + C$$

The SAXS analysis is on-going. The goal of this work is to characterize the crack size distribution in the sub-micron range, looking for thresholds in the behavior as the strain increases.

C.7. Transmission Electron Microscopy (TEM). We have set aside some samples for future testing of the level, location, and morphology of microcracking using TEM characterization. TEM requires sample preparation with the focused ion beam (FIB) in order to obtain samples of a suitable size and surface condition. A small sample is cut from the larger sample used in the mechanical tests and tomography. We have potted a sample in epoxy and stored it for future FIB and TEM work.

C.8. Conclusions. We have conducted material tests to characterize microcracking due to bending, such as might be experienced by the carbon composite materials in the starshade petals during stowing, deployment or even handling during assembly. These tests have found no large cracks (> 100 microns) at bending strains up to 0.005, the strain at which audible popping occurred. The stress-strain curves did not display any anomalies until a precipitous drop in stress at a strain of ~ 0.012 due to the formation of a transverse crack. Analysis of SAXS data is on-going which will quantify microcrack distributions at the sub-micron level.

An interpretation of these results is that failure occurs at several levels within the carbon fiber composites. At very low levels of strain, the material bends elastically. At a strain of $\sim 0.1\%$ microcracking begins to create a low density of extremely small cracks. This inference is based on the work of Bussiba et al. [Bussiba 2008a], since we have not observed these cracks in our experiments. At a strain of $\sim 0.5\%$ microcracks are sufficiently large that audible popping occurs. These cracks are less than 100 microns in size, and have no pronounced effect on the stress-strain curves. Then at a strain of $\sim 1.2\%$ a large transverse crack forms that fractures one layer of the composite leading to a large drop in the stress, but not leading to complete failure of the material. Finally, at a strain of ~ 0.22 the material fails completely due to fracture of all of the layers of the composite.

According to this interpretation, critical structural elements such as the battens which experience strains $< 0.05\%$ in stowing, deployment or operation [Kasdin 2011] would bend elastically and microcracking would not take place that could affect their performance. Provided they are handled carefully during assembly, microcracking is not an issue for them. The optical edge also experiences small strains during stowing, deployment or operation of $< 0.1\%$ because it is only ~ 0.5 mm thick. The longerons experience larger strains $\sim 0.5\%$, near the threshold for audible popping. Microcracking does occur at this level of strain, but the length of the longerons is not so critical for maintaining the critical dimensions of the petals. Even strains of $\sim 0.5\%$ are well below the threshold for failure.

Cracking may also be a concern in other areas of the starshade. We have not assessed whether cracking might happen on the sharp edge of the optical edge material. In this case, the concern is that cracking might roughen the surface due to the cracks themselves or the exposure of fibers and this roughness could cause additional light scattering. So far it appears that the material is sufficiently robust, and there is nothing to indicate that edge cracking will be a problem; we make note of it here as something related to the microcracking tests but not explicitly measured.

APPENDIX D. COMPLETE ERROR BUDGET

Random Errors		250	300	350	400	450	500	550
Segment dx	20 um	1.64E-15	6.13E-15	9.39E-15	3.83E-14	1.35E-13	3.12E-13	5.31E-13
Segment dy	20 um	2.77E-14	5.57E-14	8.96E-14	4.37E-13	1.59E-12	3.78E-12	6.59E-12
Segment in plane tilt	20 urad	2.49E-15	2.88E-14	1.50E-13	5.08E-13	9.81E-13	1.40E-12	1.64E-12
Segment Placement Total		3.18E-14	9.06E-14	2.49E-13	9.83E-13	2.71E-12	5.50E-12	8.76E-12
1 cycle/segment	15 um	6.69E-12	1.03E-11	1.02E-11	9.08E-12	7.66E-12	6.36E-12	5.20E-12
2 cycle/segment	15 um	3.79E-12	7.69E-13	1.31E-13	1.85E-13	3.24E-13	4.18E-13	4.53E-13
3 cycle/segment	10 um	2.02E-13	6.54E-14	1.63E-14	2.85E-14	5.17E-14	6.90E-14	7.70E-14
4 cycle/segment	10 um	8.08E-14	2.89E-14	7.84E-15	1.44E-14	2.66E-14	3.61E-14	4.07E-14
5 cycle/segment	10 um	4.42E-14	1.65E-14	4.71E-15	8.84E-15	1.64E-14	2.24E-14	2.53E-14
6 cycle/segment	10 um	2.82E-14	1.07E-14	3.15E-15	6.01E-15	1.12E-14	1.53E-14	1.73E-14
Segment Shape Total		1.08E-11	1.12E-11	1.04E-11	9.32E-12	8.09E-12	6.92E-12	5.81E-12
Proportional Width	5.00E-06	9.33E-15	1.81E-14	2.59E-14	3.66E-14	4.78E-14	5.94E-14	6.95E-14
Tip clip	1 mm	1.15E-13	9.57E-14	8.17E-14	7.16E-14	6.41E-14	5.78E-14	5.33E-14
Quadratic out of plane	5 mm	6.96E-17	1.08E-17	4.92E-18	1.06E-17	3.24E-16	1.74E-15	6.34E-15
In plane quadratic bend	250 um	3.98E-18	9.87E-18	1.92E-17	3.22E-17	4.81E-17	6.91E-17	9.46E-17
Non-Segment Manufacture		1.25E-13	1.14E-13	1.08E-13	1.08E-13	1.12E-13	1.19E-13	1.29E-13
Random Error Total		1.10E-11	1.14E-11	1.07E-11	1.04E-11	1.09E-11	1.25E-11	1.47E-11
Global Errors								
Segment dx	5 um	1.95E-16	1.35E-15	2.25E-15	8.40E-15	1.97E-14	3.51E-14	5.93E-14
Segment dy	5 um	2.57E-15	9.12E-15	3.19E-14	1.22E-13	2.17E-13	3.85E-13	8.61E-13
Segment in plane tilt	5 urad	2.48E-16	5.27E-15	5.25E-14	1.21E-13	1.39E-13	1.51E-13	1.91E-13
Segment Placement Total		3.01E-15	1.57E-14	8.66E-14	2.51E-13	3.76E-13	5.71E-13	1.11E-12
1 cycle/segment	5 um	8.90E-13	3.59E-12	5.12E-12	5.27E-12	3.90E-12	2.69E-12	2.03E-12
2 cycle/segment	5 um	1.47E-12	1.95E-13	3.16E-14	4.79E-14	8.56E-14	1.04E-13	1.17E-13
3 cycle/segment	3 um	1.30E-13	2.84E-14	8.05E-15	1.53E-14	2.66E-14	3.37E-14	4.03E-14
4 cycle/segment	3 um	4.28E-14	1.09E-14	3.79E-15	7.43E-15	1.28E-14	1.66E-14	2.04E-14
5 cycle/segment	3 um	2.05E-14	5.62E-15	2.24E-15	4.50E-15	7.65E-15	1.00E-14	1.24E-14
6 cycle/segment	3 um	1.21E-14	3.45E-15	1.49E-15	3.04E-15	5.13E-15	6.73E-15	8.41E-15
Segment Shape Total		2.57E-12	3.83E-12	5.17E-12	5.35E-12	4.04E-12	2.86E-12	2.23E-12
Proportional Width	5.00E-06	1.89E-14	4.74E-14	6.04E-14	6.12E-14	6.68E-14	1.03E-13	1.81E-13
Tip clip	1 mm	1.72E-13	1.29E-13	9.87E-14	1.29E-13	1.44E-13	1.31E-13	1.07E-13
Quadratic out of plane	5 mm	1.23E-16	1.71E-17	6.64E-18	2.61E-17	7.80E-16	3.78E-15	1.23E-14
In plane quadratic bend	250 um	5.36E-20	6.79E-20	1.37E-19	3.25E-19	5.89E-19	8.99E-19	1.27E-18
Non-Segment Manufacture		1.91E-13	1.77E-13	1.59E-13	1.90E-13	2.12E-13	2.37E-13	3.01E-13
Global Error Total		2.76E-12	4.03E-12	5.41E-12	5.79E-12	4.62E-12	3.67E-12	3.64E-12
Design Nominal Contrast								
TOTAL CONTRAST		5.70E-13	2.10E-13	3.03E-13	3.07E-13	3.41E-13	1.81E-13	7.10E-13
		1.43E-11	1.56E-11	1.64E-11	1.65E-11	1.59E-11	1.64E-11	1.91E-11

FIGURE 44. The complete manufacturing error budget with allocations to both random petal-to-petal errors and global systematic errors identical on every petal. Resulting contrast contribution for each term is given at 7 wavelengths over the occulter passband.

APPENDIX E. TABLE OF ACRONYMS

Acronym	Meaning
TDEM	Technology Development for Exoplanet Missions
NASA	National Aeronautics and Space Administration
JPL	Jet Propulsion Laboratory
CTE	Coefficient of Thermal Expansion
CMM	Coordinate Measuring Machine
IWA	Inner Working Angle
THEIA	Telescope for Habitable Exoplanets and Interstellar/Intergalactic Astronomy
O ₃	Oculting Ozone Observatory
NGAS	Northrop Grumman Aerospace Systems
GFRP	Graphite Fiber Reinforced Plastic
OD	Outer Diameter
ID	Inner Diameter
TOMS	Thermo-Optical Micrometeorite Shield
CNC	Computer Numerical Control
AASC	Applied Aerospace Structures Corporation
CAD	Computer Aided Design
GUI	Graphic Users Interface
PDF	Probability Distribution Function
SAXS	Small-Angle X-Ray Scattering

TABLE 6. A list of acronyms used in the report and their meanings.

REFERENCES

- [1] R.J. Vanderbei, E.J. Cady, and N.J. Kasdin. Optimal occulter design for finding extrasolar planets. *Astrophysical Journal*, 665:794–798, 2007.
- [2] D. Savransky, D. N. Spergel, N. J. Kasdin, E. J. Cady, P. D. Lisman, S. H. Pravdo, S. B. Shaklan, and Y. Fujii. Occulting ozone observatory science overview. In *Proceedings of the SPIE Astronomical Instrumentation Conference*, number 88 in 7731, 2010.
- [3] M. W. Thomson, P. D. Lisman, R. Helms, P. Walkemeyer, A. Kissil, O. Polanco, and S. Lee. Starshade design for occulter based exoplanet missions. In *Proceedings of the SPIE Astronomical Instrumentation Conference*, number 191 in 7731, 2010.
- [4] N. Jeremy Kasdin, Paul Atcheson, Matt Beasley, Rus Belikov, Morley Blouke, Eric Cady, Daniela Calzetti, Craig Copi, Steve Desch, Phil Dumont, Dennis Ebbets, Rob Egerman, Alex Fullerton, Jay Gallagher, Jim Green, Olivier Guyon, Sally Heap, Rolf Jansen, Ed Jenkins, Jim Kasting, Ritva Keski-Kuha, Marc Kuchner, Roger Lee, Don J. Lindler, Roger Linfield, Doug Lisman, Rick Lyon, John MacKenty, Sangeeta Malhotra, Mark McCaughrean, Gary Mathews, Matt Mountain, Shouleh Nikzad, Bob OConnell, William Oegerle, Sally Oey, Debbie Padgett, Behzad A Parvin, Xavier Prochaska, James Rhoads, Aki Roberge, Babak Saif, Dmitry Savransky, Paul Scowen, Sara Seager, Bernie Seery, Kenneth Sembach, Stuart Shaklan, Mike Shull, Oswald Siegmund, Nathan Smith, Remi Soummer, David Spergel, Phil Stahl, Glenn Starkman, Daniel K Stern, Domenick Tenerelli, Wesley A. Traub, John Trauger, Jason Tumlinson, Ed Turner, Bob Vanderbei, Roger Windhorst, Bruce Woodgate, and Bob Woodruff. THEIA: Telescope for habitable exoplanets and interstellar/intergalactic astronomy. http://www.astro.princeton.edu/dns/Theia/nas_theia_v14.pdf.
- [5] S. B. Shaklan, L. F. Marchen, D. Lisman, E. J. Cady, S. R. Martin, N. J. Kasdin, and P. J. Dumont. A starshade petal error budget for exo-earth detection and characterization. In *Proceedings of the SPIE Conference on Optics and Photonics*, number 38 in 8151, 2011.
- [6] Stuart B. Shaklan, M. Charley Noecker, Tiffany Glassman, Amy S. Lo, Philip J. Dumont, N. Jeremy Kasdin, Eric J. Cady, Robert Vanderbei, and Peter R. Lawson. Error budgeting and tolerancing of starshades for exoplanet detection. volume 7731, page 77312G. SPIE, 2010.
- [7] W. H. Press, S. A. Teukolsky, W. T. Vetterling, and B. P. Flannery. *Numerical recipes. The art of scientific computing*. 2007.
- [8] N. J. Kasdin, D. N. Spergel, R. J. Vanderbei, D. Lisman, S. Shaklan, M. Thomson, P. Walkemeyer, V. Bach, E. Oakes, E. Cady, S. Martin, L. Marchen, B. Macintosh, R. E. Rudd, J. Mikula, and D. Lynch. Advancing technology for starlight suppression via an external occulter. In *Society of Photo-Optical Instrumentation Engineers (SPIE) Conference Series*, volume 8151 of *Society of Photo-Optical Instrumentation Engineers (SPIE) Conference Series*, 2011.
- [9] E. Cady. Boundary diffraction wave integrals for diffraction modeling of external occulters. *Optics Express*, 20:15196–15208, July 2012.
- [10] E. Cady. *Design, Tolerancing, and Experimental Verification of Occulters for Finding Extrasolar Planets*. PhD thesis, Princeton University, 2010.
- [11] B. A. Turlach. *Bandwidth selection in kernel density estimation: a review*. CORE and Institut de Statistique, 1993.
- [12] B. W. Silverman. *Density estimation for statistics and data analysis*. 1986.
- [13] H. W. Lilliefors. On the Kolmogorov-Smirnov test for normality with mean and variance unknown. *Journal of the American Statistical Association*, 62:399–402, 1967.
- [14] M. C. Jones and D. A. Henderson. *Maximum likelihood kernel density estimation*. 2004.